Energy absorption assessment of bio-mimicked hybrid Al/PP sandwich tube: Experimental and Numerical Investigation

Moslem Rezaei Faraz[a], Hamed Ahmadi[a], Gholamhossein Liaghat[a,c,*], Samireh Vahid[b], Omid Razmkhah[c], Amirreza Tarafdar[a]

[a] *Department of Mechanical Engineering, Tarbiat Modares University, Tehran, Iran.*

[b] *School of Mechanical & Aerospace Engineering, Kingston University, London, England, United Kingdom.*

[c] *Department of Mechanical Engineering, Coventry University, Coventry, UK.*

[*]*(corresponding author: ghlia530@modares.ac.ir)*

Abstract

This paper aims to investigate quasi-static and low-velocity impact responses of three manufactured bio-inspired hybrid multi-cell aluminum and polypropylene (Al/PP) sandwich tubes experimentally and numerically. The configurations are inspired by biological structures such as the horsetail, human tendons, and spongy bone. The crushing characteristics and axial collapse of sandwich tubes are discussed and compared with the quasi-static axial behavior of single Al and PP tubes. Further investigations, based on the accuracy of simulation results of the tested specimens, using the commercial nonlinear LS-DYNA software, on the effects of inner tubes diameter and material permutation are perceived through the full-factorial approach of FE parametric study. The results revealed that, packing the Al and PP tubes as hierarchical tubes generally improves the crushing patterns of individual hollow tubes. Also, specimens with aluminum and polypropylene cores have the highest amount of specific energy absorption under quasi-static and low-velocity impact loading, respectively. Finally, considering the interaction effects between the sandwich tube components, it can be seen that sandwiching single hollow tubes generally improves important crashworthiness indicators like peak crush force, crush force efficiency, energy absorption, and specific energy absorption when compared to the sum of these parameters in single hollow tubes.

Keywords: polypropylene, sandwich tube, bio-inspired, hybrid, energy absorber, interaction effect.

1. Introduction

In recent years, demand for light energy absorbers with high energy absorption capacity has increased in the aerospace [1], transportation [2], submarine [3], civil engineering [4], and oil and gas pipeline industries [5]. As an effective energy-absorbing element, thin-walled structures have been widely used in the aforementioned industries due to their high energy absorption to weight [6-9]. In thin walled members, the kinetic energy is dissipated by gradual deformation of the structure at the collision, and only a small amount of force is imparted to the occupants [10-13]. Geometry and material properties are the most important factors for designing thin-walled energy absorbers [13-16]. Over the last decades, the axial static and dynamic deformation behaviors and laws of metallic thin-walled tubes have been the subject of many previous theoretical [17-19], numerical [20-22], and experimental studies [23-26]. Among metal materials, aluminum alloys have been extensively used to design thin-walled tubes of various shapes because of their high strength to weight, excellent load-carrying capacity and low cost [27-29]. However, it is noteworthy the mass of typical lightweight metallic energy absorbers can hardly be further reduced. Therefore, in recent decades, the use of other materials such as composite and thermoplastic materials with good energy absorption properties has increased. Thermoplastics like polypropylene have several attractive properties. They are impact resistant, lightweight, reasonably low cost, easy to construction, renewable, strain rate sensitive, temperature-sensitive, sustainable, and depending on the environment and additives [30-38]. Therefore, the interest of different industries in using such materials in structural and safety parts has grown. For example, the use of thermoplastic polymers for padding applications in the automotive sector has recently increased and motivated by various safety regulations, including the FMVSS (Federal Motor Vehicle Safety Standard) for in-vehicle collisions and the FMVSS 581 and ECE-R 42 (European regulations) for a passive bumper. However, to comply with these standards, thermoplastic materials must be designed in complex structures that, in the event of an impact, reduce the specified speed and are not harmful to occupants [30, 36].

As mentioned before, the cross-section configuration of thin-walled tubes is one of the most important factors of energy absorber design [14-16]. Many researchers have studied thin-walled tubes with various cross-sectional configurations to see if they may boost energy absorption [39-42]. For instance, Nia and Hamedani [43] compared the performance of thin-walled tubes with circular, square, triangular, and conical sections under axial quasi-static loading. They found that a tube with a circular section has the highest specific energy absorption. Circular tubes'

excellent energy absorbing capacity is mainly attributed to their series of diverse crushing failure modes, including multiple forms of folding mode, hinging, and plastic deformation [44]. Andrews et al. [45] experimentally investigated the quasi-static axial crushing modes of circular Al alloy tubes. Four failure categories were classified as concertina mode, diamond mode, mixed-mode, and Euler mode. Guillow et al. [46] systematically classified the effects of length-to-diameter (L/D) and diameter-to-thickness (D/t) ratio on quasi-static and dynamic axial crushing behaviors of circular aluminum and steel tubes.

However, single-cell thin-walled metal tubes under axial loading have some disadvantages, such as high initial peak force, low energy absorption efficiency, and impact instability. Therefore, several methods have been tried to improve structural energy absorption, such as multi-corner, multicellular structures, and the use of fillers such as foam, introduced in thin-walled structures [8, 28, 47, 48]. The internal filling is an effective way to reinforce the structure. For lightweight design, low-density fillers, such as polymeric and metallic foams, have demonstrated the considerable potential to increase further energy absorption, which has drawn increasing interest recently [49, 50]. On the other hand, previous studies on multicellular structures with different cross-sections show that these structures, due to the interaction between their components, in addition to better energy absorption, reduce the initial peak force compared to single-cell tube [51, 52]. For instance, Kim [53] has proposed innovative multi-cell profiles with an additional square element at each corner of a square column. In this study, an analytical solution for the mean crushing force was extracted, and the optimization process was performed to maximize the SEA successfully. According to the results, the amount of SEA in the new multi-cell structure has increased by 190% compared to the normal square column. Vinayagar and Kumar [10] have studied the crash performance of thin-walled tubular structures, including an outer circular tube and an inner tube with different sections. The results of this research, which has been performed as a quasi-static experimental test, show that configuration with hexagonal inner tube due to the greater number of corners have a greater ability to absorb energy. Wang and Liu [٥٤] used circular aluminum tubes in the honeycomb structure as the core. They concluded that the new honeycomb structure's load-bearing capacity and energy absorption increased compared to the honeycomb structure without the aluminum core and the structure's buckling behavior was also improved. In a study by Liu et al. [55] the impact behavior of a star core sandwich tube was investigated, they showed that the interaction between the components in the sandwich tube can significantly increase its crashworthiness as well as energy absorption. They also showed that the mean crush force in the new design is 25% higher than that of star-shaped tube.

Although these cited studies have exhibited significant energy absorption capacity, the structures have not yet been optimized. To further improve energy absorption capacity, scientists and engineers have tried to learn from biological structures-like, horsetail [56], bamboo [57], tendon [58], and human vessel [4], which, through years of evolution, have optimized their structure to adapt to various extreme environments. For instance, Zhang et al. [47] proposed a group of bionic multicellular tubes (BMCTs) inspired by the microstructure of beetle front wings. This study was performed using LS-DYNA's explicit FE code and then validated with the super-simplified fold element theory (SSFE). The results show that BMCTs showed superior crashworthiness to traditional multi-cell structures. J Hirsch [59] performed an experimental and numerical study on simple and fractal hierarchical structures inspired by spider webs and showed that the energy absorption of hierarchical fractal design under dynamic loading is better than the design of simple hierarchical, and also the second order fractal hierarchical structure (FS2) has optimal crashworthiness capability. Xiao Y et al. [56] have studied the multicellular structure inspired by the horsetail under axial loading with LS-DYNA software. The results show that the number of cells, inner wall diameter, and wall thickness of HBTS have significant effects on it has HBTS failure rate and among 6 different modes, the 16-cell geometry with the highest number of cells has the best performance in energy absorption. Liang et al. [44] considered hierarchical structures inspired by the outer layer of bone used a compression, quasi-static test to examine the properties of crushing, axial collapse, and energy absorption behaviors, mostly with hollow tubes Al circles are compared. In this research, five different configurations of hierarchical tubes with CFRP and aluminum hollow tubes have been designed. The results show that the multicellular tubes are subjected to a special progressive fold collapse and increased the energy absorption capacity of aluminum tubes, but also significantly stabilize the folding process of these tubes.

In our previous work [16], which was devoted to evaluating the energy absorption performance of hybrid multicellular sandwich tubes inspired by bio Al / GFRP with hierarchical cores, the results show that full composite sandwich tubes have the highest specific energy absorption compared to other specimens under quasi-static and low-velocity impact axial loading. In addition, the comparison between the collapse mechanisms in aluminum and composite tubes in each sandwich tube with its similar individual tube under quasi-static loading shows that the defined structure improves the collapse mechanisms in aluminum and composite tubes. Continuing the previous work, in the present study, for the first time, pure polypropylene tubes due to the ability of folding and axial collapse along with aluminum tubes, sensitivity to strain rate, impact resistance, easier construction, low cost, short manufacturing

time, and 100% recyclability has been used instead of composite tubes. The aim of this study was to investigate the energy absorption and axial collapse of hybrid multi-cell aluminum and polypropylene (Al/PP) sandwich tubes inspired by the structure of horsetail, human tendons and spongy bone under quasi-static axial load and low velocity impact (Shown in Figure 1). The energy absorption characteristics and collapse mechanisms of sandwich tubes have been compared with each other under quasi-static and low-velocity impact. Also, LS-DYNA commercial non-linear software is used to simulate the crashworthiness behavior of the fabricated sandwich tubes. Moreover, a parametric study has been conducted. The effect of the diameter of the internal and core tubes and the effect of the material used in each geometry in full factorial approach on energy absorption parameters has been investigated, relying on the accuracy of simulation of laboratory specimens. Finally, to understand the interaction effects between the components of each sandwich tube, the results of the defined parameters for each specimen are compared with the sum of individual components of that sample.

Figure 1

2.   Experimental procedure:

2.1   Structural description:

In this study, axial crushing behavior and energy absorption of three hybrid multi-cell aluminum/polypropylene (Al/PP) and full-polypropylene hierarchical sandwich tubes (second-order) with similar circular cross-sections inspired by structural patterns of the horsetail, human tendons and spongy bone. For this purpose, three similar sandwich tubes are considered with various material permutations for their components (core, internal, and external tubes). Eight PP tubes are embedded between external and internal tubes in all three specimens as core components. As shown in Figure 1, core, internal, and external tubes, regardless of their material, have external diameters of 21, 35, and 82 mm, respectively. Also, the thickness of walls in Al and PP tubes is 1 and 1.5 mm, respectively, and the height of all tubes is designated to be 90 mm. Al and PP tubes primarily underwent machining for producing specimens of mentioned dimensions. The specimens are labeled using three-letter codes, which denote the external, the core, and the internal tube materials. Also, the letters A and P represent the aluminum and polypropylene components of the sandwich structure, respectively. For example, the code APP stands for a specimen composed of an external Al tube, an internal PP tube, and its core including eight PP tubes.

2.2   Materials:

Sandwich tubes comprise of aluminum (Al) and polypropylene (PP) components. Al tubes are extruded from aluminum alloy 6061-T6, a lightweight alloy with high strength. The mechanical properties of this alloy are obtained by performing ASTM-E8/M tension tests. According to the results, density, Poisson's ratio, elastic modulus, and yield stress are 2700 kg/m3, 0.33, 70 GPA, and 260 MPa, respectively. PP tubes, because of their high impact resistance, lightweight, folding capability are used along with aluminum tubes. To obtain mechanical properties and stress-strain curve of PP tubes, they are tested according to ASTM D638 Type-I standard. These tubes' stress-strain curves and other mechanical properties are presented, respectively, in Figure 2 and Table 1.

Figure 2

Table 2

2.3   Test Procedure:

Quasi-static compression and low-velocity impact tests were carried out to evaluate the energy absorption capacity and crushing behavior of single Al and PP tubes and sandwich tubes under axial loading. Tests are conducted three times for each material permutation to ensure the reliability of results obtained for all single tubes under quasi-static loading and each sandwich tube under both loading conditions. Because of temperature effects on polypropylene, specimens are tested in an environment with a uniform temperature of 25 °C. The results obtained for each sample are averaged over three consecutive tests of each specimen. Ultimately, the energy absorption capability of single and sandwich tubes are assessed based on crack propagation behaviors, failure mechanisms, and force-displacement responses captured from both tests.

2.3.1   Quasi-static compression test:

A Universal Testing Machine (UTM) with a load cell capacity of 300 kN is used (shown in Figure 3(a)) for conducting quasi-static axial compression tests on single Al and PP tubes and hierarchical sandwich tubes. In the compression test, specimens are located between two up and bottom plates with no clamp. Also, the central axis of samples and upper and lower plates of the device coincide, and structures are loaded at a rate of 5 mm/min. For each specimen, the force and displacement curves (as a function of time) is directly extracted from the universal testing

machine and other energy absorption parameters such as peak crushing force (PCF), mean crushing force (MCF), energy absorption (EA), specific energy absorption (SEA), crush force efficiency (CFE), and crush length efficiency (CLE) are calculated based on the force-displacement curves.

2.3.2   *Low-velocity axial impact test:*

The energy absorption of the bio-inspired sandwich tubes under axial low-velocity impact loading is determined using a drop hammer testing apparatus. Schematic and details of this device and its connections are presented in Figure 3(b). After each test, the impactor returns to its initial position using the installed magnetic plane. It is worth mentioning that the defined height in this test leads to a velocity of 7.09 m/s during impact with specimens. Also, a high-speed 900 fps camera is used to capture the collapse mechanisms of each sandwich tube during loading.

Also, a 50000 g accelerometer is installed on the upper plate to measure the impactor acceleration during collide with specimens. This accelerometer is capable of recording data with a 250 kHz frequency. A CFC 500 filter cancels noises in the obtained acceleration-time curve. Then, the force-displacement curve and, consequently, energy absorption parameters can be derived via mathematical operations on the acceleration-time curve of each sandwich tube.

Figure 3

2.4   *Crashworthiness criteria:*

Some essential indicators are given below with brief explanations to improve our understanding of the crashworthiness of thin-walled structures:

2.4.1   *EA:*

Energy Absorption (EA) represents the total energy absorbed by the specimen and is equal to the area of the axial crushing force versus displacement. EA is defined as,

$$EA = \int_0^{L_c} P_{(x)} dx \tag{1}$$

Where $P_{(x)}$ is the immediate crushing force, with a function of the crushing length (L_c).

2.4.2   SEA:

Specific Energy Absorption (SEA) is defined as absorbed energy per unit mass of the structures. It is one of the important factors for comparing the energy absorption capacity of structures with different mass, which is given by,

$$SEA = EA/m \tag{2}$$

Where m is the structure's mass, obviously, for energy-absorbing structures, a higher SEA demonstrates a higher energy absorption capability.

2.4.3   MCF:

The mean crush force (MCF) is the response factor for the energy absorption capability of a structure, which is defined as,

$$MCF = EA/L_c \tag{3}$$

2.4.4   PCF:

The peak crushing force (PCF) is the maximum force during the whole loading process. Which is usually related to the first fold of the specimen. PCF is defined as,

$$PCF = max(P_{(x)}) \tag{4}$$

This parameter should be as close to the mean crush force. Otherwise, the effect of the energy absorber to protect the occupants will be reduced, and there will be a possibility of damage to the occupants and the protected contents.

2.4.5   CFE:

The crush force efficiency (CFE) is another important crashworthiness indicator, is defined as the ratio between MCF and PCF, given as

$$CFE = \frac{MCF}{PCF} \times 100 \tag{5}$$

For an ideal energy absorber, the CFE is equal to 100%.

2.4.6   CLE:

The crush length efficiency (CLE) is the ratio of crush length to the initial length of the structure. CLE is defined as,

$$CLE = \frac{L_c}{L} \times 100 \qquad\qquad\qquad\qquad\qquad\qquad\qquad (6)$$

Where Lc and L represent the crush length and the initial length of the structure, respectively.

3. Numerical simulation:

A non-linear simulation code LS-DYNA (in a double-precision mode) is used to study the deformation, interaction between components, and material permutation effects in the sandwich tubes. In the first step, Al and PP single hollow tubes are simulated individually under quasi-static axial compression to simulate sandwich tubes under two types-defined loading. Then, sandwich tubes are simulated under quasi-static loading by applying appropriate friction coefficients between sandwich tube components. Eventually, the simulation of sandwich tubes under low-velocity impact loading is conducted by introducing the strain rate effects into the mechanical properties of PP tubes.

3.1 Geometry:

As shown in Figure 4, Al and PP tubes are modeled as 4-node shell elements based on Belytschko-Tsay formulation and five integration points through the thickness. The mean value of the diameter is used for single hollow tube modeling, and then it is completed by applying 1 and 1.5 mm thickness of Al and PP tubes, respectively. The modeling ended by placing these tubes next to each other between upper and lower rigid plates, as shown in Figure 5. The optimal mesh size is chosen between 0.5-2.5 mm. The mesh independence is observed for all hollow tubes at a minimum element size of 1 mm. Therefore, the total number of elements in the external, internal, and core tubes are 22500, 9630, and 6750, respectively.

Figure 4

Figure 5

3.2 Boundary conditions:

In experimental conditions, single hollow tubes and hierarchical sandwich tubes are in contact with upper and lower rigid plates with no clamp. All degrees of freedom at the lower rigid platen is fully constrained. Also, the upper rigid platen is controlled using boundary condition BOUNDARY_PRESCRIBED_MOTION-RIGID and can only move in the vertical line. In the simulation of quasi-static axial compression, the upper rigid platen is controlled with a loading rate of 5 mm/min. The ratio of kinetic energy to internal energy for individual and sandwich tubes must be lower than

5 percent for this loading type to satisfy quasi-static loading conditions [41, 60]. The kinetic and internal energy ratios in terms of displacement for all single Al and PP tubes and three hierarchical sandwich tubes are given in Figure 6(a) and (b). As can be seen, these ratios, except for the small region at the beginning of the curves where their initial folding occurs, are lower than the determined value. On the other hand, to simulate sandwich tubes under low-velocity impact loading, the initial velocity boundary condition on the rigid upper plate is used.

Figure 6

The fundamental material model for the simulation of Al is model 123 (modified_piecewice_linear_plasticity (MAT 123)) [8]. This material model is specific to materials' elastic-plastic behavior, supports an arbitrary stress-strain curve, and depends on an arbitrary strain rate. Due to the close similarity between the behavior of PP and Al and their elastic-plastic properties, this material model can be used for simulating PP tubes. Additionally, this material model benefits from an enhanced failure model based on effective plastic strain and principal in-plane strain components.

Also, in this model, the plasticity of Al and PP is formulated as follows:

$$\sigma_y = \beta\left[\sigma_o + f_h\left(\varepsilon_{eff}^p\right)\right] \tag{7}$$

Where β represent the Cowper-Symonds strain-rate coefficient and σ_0 is the static yield stress.

$$\beta = 1 + \left(\frac{\dot{\varepsilon}}{C}\right)^{\frac{1}{P}} \tag{8}$$

Also, C and P are Cowper-Symonds material parameters. We have:

$$f_h\left(\varepsilon_{eff}^p\right) = E_P\left(\varepsilon_{eff}^p\right) \tag{9}$$

E_P= plastic hardening modulus

ε_{eff}^p= effective plastic strain

It is worth mentioning that there are two methods for defining failure and yield strains in Al and PP material models: 1- Applying the RTCL yield criterion to determine the effective plastic (or failure) strain. 2- Defining yield stress and using stress-strain curve. When stress-strain curve and yield stress are defined for the material model, the program deactivates RTCL. All parameters required for simulating single Al and PP tubes using the MAT 123 model are applied according to values in section 2.2.

3.2.1   Strain-rate effect:

According to studies [61, 62], the plastic behavior and deformations in Al tubes are not affected by the strain rate in the range of $[10^{-4}-10^3]$ ($1/_s$). Hence, no strain hardening coefficient is defined for the Al tube simulation. However, in contrast to Al material, PP tubes behavior under low-velocity impact compression is extremely influenced by strain rate, which must be considered in numerical simulation of sandwich tubes under this loading type. The maximum strain rate in sandwich tubes under low-velocity impact loading is about 1.67 (1/s). On the other hand, using the same PP material in this research as [37], the mechanical properties obtained for a strain rate of 1.67 (1/s) in this study are applied here. At the mentioned strain rate, the elastic modulus and yield stress increase by 10% and 30%, respectively, compared to quasi-static axial loading.

3.3   Contact definition:

In this study, different types of contact algorithms are defined to achieve more accurate results. CONTACT_AUTOMATIC_SINGLE_SURFACE is used for tubular elements to prevent self-penetration into other familiar elements. Moreover, CONTACT_AUTOMATIC_SURFACE_TO_SURFACE is applied for the contact of upper and lower rigid plates and the contact between components of each sandwich tube. Segment-based soft option two is utilized to prevent penetration of shell elements through upper and lower rigid plates Also, static and dynamic coefficients between all surfaces are considered 0.4 and 0.35, respectively.

4.   Results and discussion:

4.1   Quasi-static axial response of single hollow tube:

The axial crushing mode and the behavior of the bio-inspired hybrid sandwich tubes are affected by the crushing behavior of single hollow tubes. Also, to simulate sandwich tubes and understand the interactions between defined structure components, it is essential to examine the axial crush characteristics of Al and PP tubes. Besides, PP tubes are studied for the first time in this application; therefore, it is required that their crushing behavior and energy absorption level be thoroughly investigated.

Based on the previous study [46], the deformation mode and axial crushing of a hollow tube with a circular section are affected by diameter/thickness (D/t) and height/diameter (H/D) ratios. These parameters affect the number and

shape of folds, including the number of corners and regularity or irregularity of sides, and the creation of symmetric, asymmetric, and combined modes that can change the energy absorption in each tube. As discussed in section 2.1, Al and PP tubes have wall thicknesses of 1 and 1.5 mm, respectively, and the height is considered 90 mm for both. Regardless of their material, the outer diameters of external and internal tubes are 82 and 35 mm, respectively. Also, the outer diameter of core PP tubes is 21 mm. In Table 2, the ratios (D/t) and (H/D) are proposed for Al and PP tubes.

Table 2

When Al and PP tubes are axially compressed, they undergo plastic deformation due to local buckling. These plastic deformations lead to folding patterns and plastic hinges that absorb kinetic energy transferred to tubes. As mentioned above, the folding patterns of external and internal tubes are different because of different diameter/thickness (D/t) and height/diameter (H/D) ratios. As shown in Figure 7(a), the internal Al tube in the APA sandwich tube exhibits an asymmetric mixed crushing mode. The first fold appears on the head of this tube in axisymmetric (concertina) mode, and in the following, four non-axisymmetric folds (Diamond 3-lobe) with three circumferential corners (N=3) and regular sides are created.

According to Figure 7(b), in the crushed model of external Al tube in APA and APP specimens, three diamond folds (Diamond 3-lobe) with three circumferential corners (N=3) are observed. Because of manufacturing defects in this tube, the first and third folds are accompanied by circumferential and longitudinal cracks, respectively. Despite the formation of these cracks, the N-gon that appeared during the folding process (Figure 7(b2)) is an irregular polygon. Based on observations, as (D/t) and (D/H) ratios increased, the concertina mode of Al tubes vanished, and the number of folds in the external Al tube decreased compared to the internal Al tube. Also, in contrast to the internal tube, the N-gon associated with diamond folds in the outer tube has irregular sides.

When the numerical model is compared with the tested specimen, it is observed for both Al tubes that the numerical model could successfully predict crushing modes and the number of folds and their locations (see Figure 7).

Figure 7

By examining the collapse mechanisms of PP tubes shown in Figure 8(a) and (b), the core (in APA, APP, and PPP specimens) and internal tube (in APP and PPP specimens) are deformed by exhibiting a non-axisymmetric diamond mode (Diamond 2-lobe) with two circumferential corners (N=2). In these tubes, the diamond mode shapes are similar; however, by comparing Figure 8(a) and (b), it is found that the number of folds is reduced by increasing the diameter

of PP tubes. Moreover, the deformation mode of the external tube in the PPP arrangement (as shown in Figure 8(c)) is a non-axisymmetric diamond (Diamond 3-lobe) with three circumferential corners (N=3).

As can be observed, similar to Al tubes, the number of folds in PP tubes increases by a reduction in the tube diameter. However, in PP tubes, in contrast to Al tubes, a lower diameter did not cause the formation of concertina mode and decreased the number of corners for diamond-mode N-gon from N=3 to N=2. Also, in the external PP tube with a larger thickness, no crack is formed in plastic hinges due to the higher polypropylene elasticity than aluminum, and the resulting N-gon is more regular. Their length increases after the quasi-static compression test regarding the elasticity and resiliency of polypropylene tubes. As shown in Figure 8(a2), (b2), and (c2) the core, internal, and external tubes after quasi-static loading have final lengths of 64 mm, 66 mm, and 71 mm, respectively. By comparing the numerical and tested specimens of PP tubes, it is observed that there is a good agreement in terms of the number of folds and their modes, and the numerical model could well predict their unknown behavior.

Figure 8

4.1.1   Crashworthiness evaluation:

After examining the axial crushing and plastic deformation of hollow tubes in the previous section, this section examines the force-displacement curves and other energy absorption parameters.

In Figure 9 and Table 3, respectively, the force-displacement curves and critical energy absorption parameters are suggested for two hollow Al tubes experimentally and numerically. It should be noted that experimental values of energy absorption parameters (shown in Table 3) are the average of three tests repeated on each tube. Overall, the numerical and experimental force-displacement curves are similar for both tubes. They can be divided into three regions: the first is the elastic region spans from the beginning of the curve up to the initial peak point. The second region is for plastic deformation, starting from the initial peak and continuing up to the third region. The third region is attributed to the specimen's condition that becomes fully dense under compression, exhibiting a rigid-like state. The experimental value of the initial peak force for the external Al tube is 3.84 times that of the internal tube due to its larger diameter. Also, this peak forces for internal and external tubes have occurred at displacements 1.85 mm and 1.96 mm, respectively. As can be observed, the folding mode and its location are demonstrated on the experimental

force-displacement curves (see Figure 9). After the initial peak, the force levels of internal and external tubes decreased by 54% and 70%, reaching the first minimum points at displacements 4.22 mm and 7.15 mm, respectively. One of the reasons for the greater force drop in the external Al tube can be the crack occurrence in the first plastic hinge. After the first valley, the force-displacement curves of both tubes fluctuate around the MCF. The fluctuation level of the curve is higher for the internal tube due to concertina mode and non-axisymmetric diamond modes with more regular sides. On the other hand, it is observed that the two peaks for the first and third folds in the force-displacement curve of the external tube are far less than the second peak associated with the second fold due to cracking. Despite higher force drop after the initial peak and the presence of cracks in the plastic hinges, because of the larger diameter of the external tube, its experimental MCF is 2.29 times that of the internal tube.

Although PCF and MCF in the external tube are significantly higher, the CFE value in the internal tube is more desirable due to concertina mode, more regular sides of diamond folds, and lack of cracking in plastic hinges. Its experimental value is 1.67 times the value in the external tube. On the other hand, opposed to CFE, the experimental value of CLE in the external tube is 1.11 times the internal tube. An increase in crushing length of the external tube relative to the internal one can be due to cracks in first and third plastic hinges and more irregular diamond mode; so that corners of first and third folds in this tube do not coincide while in the internal tube, corners of second and fourth diamond folds, as well as third and fifth ones coincide each other. This is the reason for the rigidity of the internal tube with a lower displacement.

Figure 9

Table 3

Considering the higher CLE and the MCF in the external tube, the experimental value of EA obtained from the force-displacement curve of this specimen (shown in Figure 10(a)) is 2.46 times that of the internal tube. The experimental values of this parameter for external and internal tubes are 981.75 J and 398.96 J, respectively (the differences between experimental and numerical results for external and internal tubes are 3.5% and 2.47%, respectively). As can be observed, the EA curve slope for both tubes has the maximum value at the beginning in the elastic deformation region. On the other hand, EA curve slope of external tube associated with first and third folds at displacements 7-26 mm and from 43 mm to the end are significantly lower than displacement between 26-43 mm, where the second fold occurs. Based on the SEA values in Figure 10(b), it is observed that in contrast to absorbed

energy, the experimental value of this parameter in the internal tube is 1.07 times the value in the external one. This can be the presence of concertina mode and a higher number of more regular diamond folds (also, the differences of this parameter between numerical and experimental results for internal and external tubes are 2.47% and 3.53%, respectively).

Figure 10

According to the force-displacement curves of PP tubes in Figure 11, it can be Find out that trend of these curves is similar to the relevant curves in Al tubes, which can be because of similar axial crushing modes between PP and Al tubes. The location of each fold on the experimental force-displacement curve is shown for three PP tubes. In numerical force-displacement curves of all three tubes, there are local fluctuations due to the high elasticity of PP that can be limited by applying a more robust filter.

Based on energy absorption results in Table 4 and Figure 11, it can be observed that in PP tubes, as the (D/t) ratio increases and (H/D) ratio decreases, the PCF, MCF, and fluctuation of force-displacement curve increase. Also, with mentioned changes in (D/t) and (H/D) ratios, the curve slope in the elastic region increases like the PCF and MCF contrary to Al tubes. The initial peak forces in the core, internal, and external tubes have occurred at displacements 5.51 mm, 4.83 mm, and 2.96 mm, respectively. After the initial peak, the force drops up to the first minimum points are 72%, 78%, and 76% for the core, internal, and external tubes, respectively; these values are significantly higher in two external and internal PP tubes than Al tubes.

The experimental results for the PCF of PP tubes show that in the external tube, it is 3.33 and 1.69 times its value in core and internal tubes, respectively. After the first valley, which occurs at displacements 8.91 mm, 9.85 mm, and 10.48 mm, for core, internal, and external tubes, respectively, the curve fluctuates around the MCF. The experimental MCF of the external tube is 3.81 and 2.32 times the value in core and internal tubes, respectively. It should be noted that despite the larger thickness of external and internal PP tubes, mean crushing and peak forces in these tubes are far less than similar Al tubes.

As opposed to observations in Al tubes, the CFE of the external PP tube is higher than the two other tubes so that the experimental CFE in the external tube is 1.14 and 1.37 times the value in internal and core tubes, respectively. The reason behind this can be diamond-type folding with a higher number of sides than two other tubes and lower force

drop in the external tube after initial peak force compared with the core tube. After examining and comparing CLE in three tubes, it is found that the experimental value of this parameter is highest in the internal tube and almost equal in two other tubes. After comparing CLE results in PP and Al tubes, it can be observed that in contrast to Al tubes, the external PP tube has a lower crushing length than the internal one. Also, despite their larger thickness, PP tubes have a higher crushing length than Al tubes because of their higher elasticity.

Figure 11

Table 4

Based on force-displacement curves, the EA and SEA parameters results for PP tubes are given in Figure 12. In Figure 12(a), it can be seen that in a similar trend to Al tubes, the slope of the EA-displacement curve is maximum initially. According to this curve, the energy absorption level increases whit increasing tube diameter. The values of this parameter are 173 J, 76.3 J, and 45.64 J for the external, internal, and core tubes, respectively. Moreover, the obtained values in numerical simulation for external, internal, and core tubes are 168.05 J, 76.28 J, and 39.1 J, respectively (the differences between them for the core, internal, and external tubes are 6.63%, 0.05%, and 2.9%, respectively). Besides, the fluctuations of this curve, similar to the force-displacement curve, is higher for the external tube than the two other tubes.

Based on the experimental SEA curve in Figure 12(b), the resulted values of this parameter, contrary to EA results, are inversely varied with the diameter (like Al tubes), and the maximum SEA is for the core tube with a value of 7.61 J/gr. Also, the experimental SEAs for the internal and external tubes are 5.87 J/gr and 4.44 J/gr, respectively. The larger number of folds in the core tube can be one of the reasons for a larger SEA of this tube than two other ones (numerical and experimental results show an acceptable agreement and the differences between numerical and experimental SEA values for the core, internal, and external tubes are 2.76%, 0.2%, and 3.15%, respectively).

Figure 12

4.2 Quasi-static axial compression of bio-inspired hybrid sandwich tubes:

In the previous section, the results of single Al and PP tubes are studied. Based on the results, the folding patterns for axial crushing of three PP tubes and external Al tube are formed in non-axisymmetric diamond modes. Furthermore, the axial crushing mode in the internal Al tube is a mixed concertina and diamond mode. Also, examining

the critical energy absorption parameters showed that the SEA, EA, and MCF of Al tubes are significantly higher than PP tubes. On the other hand, the PCF in PP tubes is less, and their crushing length is far more than in Al tubes. Regarding the CFE parameter, although this value is highest in the internal Al tube among all other hollow tubes, it is significantly lower in the external Al tube than the core and internal PP tubes. Finally, by examining the obtained results for crushing folding modes of hollow tubes, the force-displacement curves, and critical energy absorption parameters in numerical and experimental simulations, it is discovered that the defined numerical model could predict the axial crushing behavior of hollow tubes properly.

4.2.1   *Crashworthiness characteristics:*

In the following, the experimental and numerical results of three bio-inspired hybrid multi-cell sandwich tubes (APA, APP, and PPP) under quasi-static axial compression will be analyzed to determine the effects of hollow tubes' material on axial crushing behavior of sandwich structures and their critical energy absorption parameters. The obtained results in force-displacement curves and critical energy absorption parameters of each specimen are the averages of three iterations. Also, to understand the effect of interaction between components of defined geometries, the PCF, MCF, EA, SEA, and CFE parameters for three sandwich tubes are compared with the sum of these parameters in their components (including internal and external tubes and eight tubes of the core).

By examining the trend of force-displacement curves for APA and APP hybrid specimens (as shown in Figure 13 and Figure 14, respectively), it can be noted that the curve of APA, in contrast to APP, is strongly affected by the behavior of the force-displacement curve of the external Al tube (demonstrated in Figure 9(b)); this holds for the PPP curve as well (see Figure 15). Although the force-displacement curve of PPP experiences lower fluctuations due to interactions between its components, it is significantly similar to the external PP tube curve in Figure 11(c). On the other hand, an overview of three force-displacement curves related to sandwich tubes under axial quasi-static compression, similar to force-displacement curves of the hollow tube, we can separate them into three elastic, progressive folding, and dense (rigid) regions. Furthermore, it is observed that their numerical force-displacement curves have local fluctuations due to the presence of PP components with low elastic modulus.

Concerning the force-displacement curves of Figure 13, Figure 14, and Figure 15, it can be seen that the PCF for all three specimens occurs at displacements lower than 5 mm. In these curves, the elastic region has ended at displacements 3.4 mm, 2.27 mm, and 4.21 mm for APA, APP, and PPP, respectively. As stated for hollow tubes, the

force-displacement curve of Al tubes has a higher slope in the elastic region than PP tubes. However, in hybrid sandwich tubes, despite a higher PP component in PAP than APA, the force-displacement curve in the elastic region has a higher slope for APP, and PCF occurs at lower displacements.

Figure 13

Figure 14

Figure 15

The energy absorption parameters proposed in Table 5 show that the highest experimental value of PCF 46.37 kN is for APP, higher than that of external Al, APA, and PPP tubes by 6.26 kN, 4.85 kN, and 28.25 kN, respectively. After reaching the initial peak point and entering the plastic deformation region, the force magnitudes in APA, APP, and PPP curves have reduced by 57.1%, 54.59%, and 55.29%, respectively, up to the first valley. This force drop is significantly lower than the three PP and external Al tubes examined in the previous section. Moreover, it is observed that by replacing the Al tube in APA with an internal PP tube in APP, the force-displacement curve descends less significantly.

The force-displacement curve fluctuated around MCF value after passing the first valley at displacements 7.42 mm, 7.09 mm, and 8.89 mm, respectively, for APA, APP, and PPP tubes. According to Table 5, similar to the PCF, the highest experimental MCF is obtained for APP equals 24.05 kN, higher than this value in external Al, APA, and PPP tubes by about 8.86 kN, 0.8 kN, and 14.07 kN, respectively.

Also, the CFE results show that this parameter in all three sandwich tubes is higher than 50%; so that CFE of APA and PPP, which is almost the same, is 6.87% higher than that of APP and is 32.0% and 19.61% higher than external Al and PP tubes, respectively. As discussed in section 4.1.2, the CFE of the internal Al tube is significantly higher than similar PP one. Therefore, one reason for decreased CFE of APP relative to APA is the internal Al tube replacement by an internal PP tube. By inspecting the CLE results in Table 5, it is revealed that crushing length has the highest value in APA, 5.02% and 4.25% higher than APP and PPP, respectively. PP tubes with larger thickness in APP and PPP lead to a decreased crushing length than APA.

The results of two EA and SEA parameters obtained from experimental and numerical force-displacement curves for three APA, APP, and PPP sandwich tubes are given in Figure 16, respectively. Like energy absorption curves of single hollow tubes, the curve slope has the maximum value at the beginning for all three curves, which is associated

with the region for the start of elastic deformation. In PPP sandwich tube, although the curve slope is high at the beginning compared with two other arrangements, it decreases significantly after starting the plastic deformation, which indicates the lower performance of this specimen in energy absorption. The mean slopes of the experimental energy absorption curves for APA, APP, and PPP are 22.96 J/mm, 24.77 J/mm, and 9.99 J/mm, respectively. According to the EA curve in Figure 16(a), the experimental value of absorbed energy by APP is 1517.85 J, higher than external Al, APA, and PPP tubes by 536.1 J, 6.69 J, and 899.03 J, respectively. In the meantime, it is observed that PCF and MCF in APP are significantly higher than others; however, because of the lower crushing length than APA, there is a slight difference in absorbed energy of these two (also, the differences between numerical and experimental values of this parameter for APA, APP, and PPP are 4%, 5.4%, and 4.3%, respectively). By examining the curve in Figure 16(b), it is found that APP has the highest SEA, and the experimental value of this parameter is 1.25 and 2.08 times that of APA and PPP, respectively. Although replacing the Al tube in APA with an internal PP tube in APP causes a 20.22% increase in this parameter, SEA in these two sandwich tubes, in contrast to energy absorption and load carrying capacity, decreases compared to external Al tube. However, contrary to other hybrid specimens, the SEA of PPP increases by 28.27% compared with the external PP tube. Also, based on the results, there is a good agreement between numerical and experimental results in terms of this parameter, and the errors between numerical and experimental data for APA, APP, and PPP are 2.7%, 5.1%, and 4.2%, respectively.

Table 5

Figure 16

4.2.2   Quasi-static post-crushing morphologies of bio-inspired hybrid sandwich tubes:

The collapsed model of the hybrid sandwich tubes APA is illustrated in Figure 17. In this specimen, the first fold of the external Al tube is formed in the upper section in concertina mode. The three next folds of this tube are non-axisymmetric diamond modes (Diamond 4-lobe) with four corners (N=4). Comparing the folding mode of this tube in APA (see Figure 17(a1)) with a similar hollow tube (see Figure 7(b)) shows that the tube in APA has a concertina mode, in addition to more diamond folds, which have more regular sides. On the other hand, the non-axisymmetric diamond mode changed from Diamond 3-lobe in the single hollow tube to Diamond 4-lobe in the APA. Moreover, due to interaction with core tubes, no crack is formed in contrast to single hollow tubes. In the internal tube of this specimen, four non-axisymmetric diamond folds (Diamond 3-lobe) are formed, with two folds in the upper section having regular sides and other folds having irregular sides. However, comparing the crushing mechanisms in the

internal Al tube of APA (Figure 17(a3)) with a similar hollow tube of the Figure 7(a) shows that the concertina mode in the hollow tube has been eliminated in the internal tube of APA and sides of non-axisymmetric diamond folds are more regular. Furthermore, Figure 17(a4) shows that core tubes in this specimen are extremely crushed.

For more accurate investigation of the effects of interaction between APA components on critical energy absorption parameters, the difference between resulting PCF, MCF, EA, SEA, and CFE for this specimen and the sum of individual components, including internal and external Al tubes and eight PP tubes of the core, is shown in Figure 18. For instance, the PCF in APA is 41.58 kN, and the sum of component-related parameters is 40.11 + 10.45 + (8 * 1.54) = 62.88 kN. Therefore, as shown in Figure 18, sandwiching hollow tubes with APA arrangement positively affects PCF and causes a 33.44% decrease in this parameter compared with the sum of peak forces of individual hollow tubes. Opposing to peak force improvement, the sandwich tube with APA arrangement leads to a 12.69%, 13.45%, and 13.39% decrease in MCF, EA, and SEA, respectively, compared to the sum of the parameters obtained for the sum of individual components. On the other hand, sandwiching a single tube in APA form has decreased MCF, but by decreasing peak force to a great extent, this leads to a 32.04% increase in CFE compared to the sum of CFEs of APA components.

Hence, it can be concluded that although the interaction between components of APA has enhanced folding mechanisms of external tube and PCF and CFE values, its destructive effects on two other components, especially internal tube, decreased MCF, EA, and SEA compared to the case in which these tubes separately underwent quasi-static axial compression test.

Figure 17

Figure 18

By evaluating the axial crushing mechanisms of the hybrid APP specimen in Figure 19, it can be noted that the external Al tube is folded in non-axisymmetric diamond mode (Diamond 4-lobe). Although there is no concertina mode in the external Al tube of APP in contrast to APA, the sides of folding mode in this tube are more regular than the similar tube in APA. On the other hand, by comparing the crushing mechanisms in the external tube of APP (see Figure 19(a1)) with a similar Al hollow tube (see Figure 7(b)), it can be concluded that interaction between APP components has increased the number of non-axisymmetric diamond folds in this sandwich tube compared to hollow tube. The resulting N-gon has more number of and more regular sides. In addition to mentioned above, Figure 19(a1)

indicates that longitudinal cracks are formed in the external Al tube of APP, while this is not observed in the same component of APA. The reason is the thicker internal PP tube of APP relative to the internal Al tube of APA. Also, evaluation of axial crushing mechanisms of the internal tube in this specimen shows that in addition to an increase in folds from three in the similar hollow tube (see Figure 7(a)) to four in APP, the non-axisymmetric diamond folds change from Diamond 2-lobe in the hollow tube to Diamond 3-lobe (as shown in Figure 19(a2)). It is worth mentioning that because of the interaction between this tube and core tubes, the formed sides in diamond modes are more irregular than the hollow tube. Therefore, it can be argued that the interaction between APP components has a sound effect on crushing behavior and crushing mechanisms in both internal and external tubes compared with similar single hollow tubes; this causes a larger energy absorption of these two tubes in the sandwich structure. Hence, sandwiching components with APP arrangement can decrease PCF by 15.74% and increase MCF, EA, SEA, and CFE by 14.6%, 6.65%, 14.72%, and 37.09%, respectively, relative to the sum of parameters associated with every single hollow tube, as shown in Figure 18. According to Figure 17 and Figure 19, the core tubes of APP, thanks to lower crushing relative to similar tubes in APA, could bring more contact with external and internal tubes, causing a more regular folding process and higher energy absorption.

After examining the crushing mechanisms and modes in hybrid sandwich tubes under quasi-static axial compression, we then analyze the crushing mechanisms of the PPP sandwich tube, as illustrated in Figure 20. By comparing Figure 8(c) and Figure 20(a1), we can deduce that the hierarchical structure of PPP creates concertina mode in external PP tube and increases the number of sides of non-axisymmetric diamond folds. The mode shapes have changed from Diamond 3-lobe in the similar hollow tube to Diamond 4-lobe. Also, based on Figure 20(a3), it can be seen that the internal tube of PPP exhibits a mixed-mode folding so that one diamond fold (Diamond 2-lobe) is formed at the upper region and two other diamond folds (Diamond 3-lobe) at the lower region of the tube. Moreover, comparing collapse mechanisms between two internal PP tubes in PPP and APP (Figure 19(a3), and Figure 20(a3)) indicates that due to the larger number of Diamond 3-lobe folds, the interaction between APP components has a more desirable effect on the internal tube. Also, the crushing of core tubes has reduced after adding internal and external PP tubes.

Figure 19

Figure 20

As shown in Figure 18, sandwiching PP components in PPP hierarchical structure causes an appropriate interaction between its hollow components, which can decrease PCF by 11.52% and increase MCF, EA, SEA, and CFE by 23.36%, 2%, 2%, and 34.49%, respectively, relative to the sum of these parameters in individual hollow tubes. It can be observed that even though crushing force in sandwich mode is significantly higher than the sum of this parameter in hollow tubular components, because of the lower crushing length of the sandwich tube compared to hollow PP tubes, the effects of components interaction on increasing EA and SEA are insignificant.

Finally, by comparing the numerical and experimental collapsed models of three defined specimens in Figure 17, Figure 19, and Figure 20, it can be observed that there is good agreement between shape and number of folds in sandwich tubes. Furthermore, it is seen that despite the great residue height of PP components in APP, the residue height of collapsed model of the external Al tube in APA is higher. Also, PPP, APP, and APA have the greatest residue length of PP components, respectively, as the number of Al components decreases.

4.2.3   Effects of designing parameters on quasi-static response:

After analysing bio-inspired sandwich tubes' axial crushing and energy absorption behavior under quasi-static compression, other effective factors on their energy absorption behavior are studied numerically. The studied factors in the numerical investigation are the effect of diameters of core and internal tubes and different material permutations (for core, external, and internal tubes). The full factorial approach is employed for material permutations in the numerical analysis, and external tube diameter is considered constant. For this purpose, as shown in Table 6 and Figure 21, three geometries with different diameters of core and internal tubes are proposed (D indicates the inner diameter of a tube). Like experimental specimens, the thicknesses of all Al and PP tubes are 1 and 1.5 mm, respectively, and the height of all is designated to be 90 mm. Eight specimens with different material permutations (AAA, AAP, APA, APP, PAA, PAP, PPA, and PPP) are defined. To better understand the effects of the diameter and material of internal and core tubes, the resulting energy absorption parameters, including PCF, MCF, EA, SEA, CFE, CLE, and force-displacement curves are studied for each specimen.

Table 6

Figure 21

Comparing the results obtained from force-displacement curves in Figure 22(a), (b), and (c) and Table 7, indicates that material and number of hollow core tubes have significant effects on energy absorption and fluctuations of force-

displacement curves in specimens of the same configuration. Comparison of force-displacement curves for specimens with the same configuration indicates that curve fluctuations and their slope in the elastic region of sandwich tubes with Al cores (AAA, AAP, PAA, and PAP) are higher than others. On the other hand, most sandwich tubes with PP cores (APA, APP, PPA, and PPP) have a crushing length higher than other specimens due to their higher elasticity.

Figure 22

Examination of force-displacement curves for sandwich tubes with Al cores and the same configuration shows that specimens of more Al components exhibit a greater slope in the elastic region. For all three configurations, the curve slopes in the elastic regions of specimens AAA, AAP, PAA, and PAP are, respectively, highest among eight defined specimens. Also, comparing the trend of force-displacement curves for specimens of the same configuration shows that external tube material has a dominant effect on the curve in a way that sandwich tubes with the external tube of a similar material have the same fluctuations. The results show that those with Al cores (AAA-AAP-PAA-PAP) have the highest PCF, MCF, EA, and SEA (see Figure 22).

Moreover, by comparing the mentioned parameters between sandwich tubes with Al cores of the same external and internal tube material and different configurations, it can be concluded that as the number of core tubes increases, the values of these parameters increase from configuration 1 to configuration 3. The variations of CFE in both AAA and AAP are the same as the four mentioned parameters. However, in PAP of configuration 3, global buckling occurs in hollow-core tubes because of low ratios of (D/t) and (D/H), and therefore, the force level decreases after reaching an initial peak. Although MCF is highest in PAP material permutation of configuration 3, the CFE value in this configuration is lower than the two others. On the other hand, the CFE value of PAP with configuration 1 is suitable despite higher (D/t) and (D/H) values in core tubes than the other two configurations; this is because of the inability of internal and external PP tubes to prevent global buckling of core tubes. However, for PAA, an internal Al tube could prevent global buckling in core tubes of configuration 3 to some extent, and the CFE of this specimen with configuration 3 has the highest value.

Analysis and comparison of the resulting parameters among sandwich tubes with Al cores and the same configuration illuminate that PCF and MCF decrease by changing the external and internal Al tubes into PP. Moreover, the EA values in these specimens of configurations 2 and 3 exhibit variations similar to PCF and MCF; replacing Al tubes with internal and external PP tubes leads to decreased EA.

On the other hand, sandwiching hollow tubes with Al cores in configuration 1 has led to the lowest EA for AAA because of its lower crushing length than the other three specimens. Also, the highest EA values with this configuration are, respectively, for PAA, AAP, and PAP. Moreover, by examining SEA for sandwich tubes of Al cores and the same configuration (as shown in Figure 22(d)), it is revealed that for configuration 1, sandwich tubes with external PP tube (PAP and PAA) have higher SEA than AAA and AAP. However, as mentioned above, for configuration 3, PAP and PAA have the lowest SEA among the four specimens due to global buckling. Regarding the importance of SEA, Figure 23 illustrates the collapsed numerical models of specimens with the highest SEA among all defined ones with configurations 1, 2, and 3, which are, respectively, PAP, PAA, and AAA.

Furthermore, the results for sandwich tubes with PP core (APA, APP, PPA, and PPP) demonstrate that similar to sandwich tubes with Al core, MCF and EA increase for each specimen with an increase in the number of hollow core tubes from configuration 1 to configuration 3. Moreover, PCF and SEA in APA and PPA specimens vary similarly to EA and MCF. The derived results for CFE parameter in specimens whit PP cores in configuration 3 indicate that due to high MCF compared with other two configurations and lack of global buckling after first force peak in hollow-core tubes, sandwiching each of these specimens as configuration 3 increases CFE. Comparing the force-displacement curves and PCF, MCF, EA, and SEA parameters in APA, APP, PPA, and PPP sandwich tubes with the same configuration shows that similar to specimens with Al cores, the force-displacement curve of specimens with the external tube of the same material has a similar trend. Also, a reduction in the number of Al components in sandwich tubes with PP core in each configuration, in addition to decreasing fluctuations of the force-displacement curve and increasing the crushing length of most specimens, decreases MCF and EA parameters; in each configuration, these two parameters are highest in, respectively, APA, APP, PPA, and PPP specimens. On the other hand, PCF and SEA of these specimens in configurations 1 and 3 vary the same way as MCF and EA. However, in configuration 2, the highest PCF and SEA are for APP specimen in which the Al component is fewer than in APA. Moreover, comparing the CFE results in sandwich tubes with PP cores and similar configurations illuminates that among defined specimens, both configurations 1 and 2, those with internal Al tube (PPA and APA) have the highest CFE; but, in configuration 3, PPA and PPP have the highest CFE. As mentioned above, as the number of Al components decreases in these four specimens, crushing length increases. Among specimens with configurations 1 and 3, PPP and PPA have a higher crushing length than APA and PPP. However, in configuration 2, PPP, APA, PPA, and APP respectively have the highest crushing length.

Table 7

Figure 23

4.2.4   Interaction effect between sandwich tube components under quasi-static loading:

In this section, the interaction effects between the components of sandwich tubes defined in the numerical study (see Figure 21), under quasi-static axial compression are investigated. For this purpose, as shown in Figure 24(a) and (b), the value of change in the amount of PCF, MCF, CFE, EA, and SEA parameters for each sandwich tube compared to the sum of the results of each parameter in the relevant components, including the tube external and internal and core tubes are compared. To do this, the force-displacement diagrams of the sum obtained from the numerical simulation of single hollow tubes in each specimen are added together for the same amount of displacement and the same boundary condition with the respective sandwich tubes. For example, for the APA specimen defined in configuration 3, the force-displacement curve of the components is the sum of the two force-displacement curves of the external and internal aluminum tubes and 16 times the force-displacement curve of the polypropylene single hollow core tube.

After obtaining the force-displacement diagram of the total components in each sample, the values of the mentioned parameters were calculated and compared with the values of the same parameter in the respective sandwich tube. According to the results shown in Figure 24(a), sandwiching single tubes with each material permutation and in three configurations has reduced the PCF and increased the amount of CFE compared to the sum of these parameters in the components of the respective sandwich tube. For all samples with different material permutations, configuration 1 produced the largest reduction in the PCF parameter.

Also, by examining the MCF results in Figure 24(a) and the EA and SEA parameters in Figure 24(b), it can be seen that the sandwiching of components as configurations 2 and 3 in most of the defined specimens, except for the APA and PPA, has increased with the sum of these parameters in the respective components. However, sandwiching single hollow tubes as configuration 1 in most samples has reduced the amount of MCF relative to the sum of this parameter in its components. On the other hand, the largest increase in CFE and MCF, EA and SEA parameters occurred in all sandwich tubes with configuration 3. This phenomenon is affected by three reasons: 1- Low (D/t) and (D/H) ratios of single hollow core tubes in configuration 3 have caused these tubes to have global buckling if they are subjected to quasi-static axial compression alone and absorb very little energy. However, by sandwiching this single hollow tube

in configuration 3, the proper interaction between the components of this phenomenon has been partially eliminated. 2- Improving the shape of collapse modes in external and internal hollow tubes. 3- Another factor is the high interaction and friction between the components, due to less space between the single hollow tubes in configuration 3 than the other two configurations, and especially configuration 1. This phenomenon can increase the amount of energy absorbed in the structure and naturally have the results of MCF, CFE, EA, and SEA parameters in the defined samples relative to the sum of the relevant components (For instance, the crushing mode of the AAA specimen in configuration 3 is shown in Figure 25). As a result, it can be stated that the interaction between the sandwich tube components in configurations 3 and 1 has the greatest and least effect on the major energy absorption parameters, respectively. By examining the defined specimens with the same configuration and different materials permutation, it is discovered that, for all three defined configurations, sandwich tubes with aluminum and polypropylene cores have the lowest and highest reduction in the amount of PCF, respectively, when compared to the sum of these parameters. In addition, the difference in MCF, EA, and SEA parameters between the samples classified as configuration 1 and 3 in sandwich tubes and the total of their components, sandwich tubes with aluminum cores, is greater than in other samples with the same configuration.

Figure 24

Figure 25

4.3   Low-velocity axial crushing behavior of bio-inspired hybrid sandwich tubes:

Three APA, APP, and PPP specimens underwent low-velocity impact loading to figure out the dynamic response of the defined hierarchical sandwich tubes. As mentioned in section 2.3.2, the mass of the impactor and the height from specimens will produce kinetic energy of 1057.86 J during the collision. In this segment, to understand the sandwich tubes' behavior and the effect of hollow tubes' material, the results of numerical and experimental tests, including force-displacement curves, energy absorption, plastic deformations, and crushing mechanisms, are discussed. For studying the effects of strain rate in sandwich structures under low-velocity impact loading, PCF, MCF, EA, and SEA parameters for each specimen are compared with the results of each parameter in a similar specimen under quasi-static compression test. In each section, the agreement between experimental and numerical results is examined.

4.3.1   Crashworthiness characteristics:

Comparing the force-displacement curves for three sandwich tubes under low-velocity impact loading (shown in Figure 26), shows that all three curves have a similar trend. These curves can be separated into three elastic, progressive buckling, and unloading regions [8]. In the force-displacement curves, contrary to obtained curves in quasi-static loading, the curve increases in a fluctuating manner after reaching the initial peak. After reaching its secondary peak, it reduces. In the end, the imposed kinetic energy becomes zero due to the plastic deformation of the specimen and the friction between the specimen and upper and lower plates. According to force-displacement curves, as PP components in three sandwich tubes increase, the initial and secondary peak forces occur in higher displacement, and the curve slope decreases in the elastic region, and its fluctuations increase. The initial and second peak forces of APA, APP, and PPP specimens occurred at displacements 1.53-8.43 mm, 1.58-8.53 mm, and 3.07-15.98 mm, respectively. Comparing the numerical and experimental force-displacement curves for all three specimens shows that the numerical model could correctly predict the trend of force-displacement curves in most points. But, fluctuations of experimental and numerical curves do not agree with each other in the ending region of curves for APP and PPP specimens.

Figure 26

Based on the energy absorption results in Table 8, for three sandwich tubes, it can be concluded that the highest CLE is for PPP in contrast to obtained results in quasi-static compression loading. However, the APP specimen has the lowest crushing length despite more PP components than the APA specimen and is similar to quasi-static loading. According to the results, it is noted that the highest initial and second peak forces and MCF increase by a rise in the number of Al components of sandwich tubes. The maximum of these parameters are obtained for APA, APP, and PPP sandwich tubes, respectively. Similar to obtained results in quasi-static compression loading, the PCF and MCF are lowest in PPP specimen under low-velocity impact compression, this specimen has the highest CFE value.

The EA and SEA results for three defined tubes (shown in Figure 26(d) and Figure 27) that are derived from relevant force-displacement curves show that due to lower force of APP specimen compared to APA sandwich tube and lower crushing length than two APA and PPP specimens, the EA and SEA, similar to CFE parameter, are lowest in this specimen. Moreover, the APA sample has the highest EA value and the PPP specimen has the highest SEA value. The experimental EA values in APA, APP, and PPP sandwich tubes are, respectively, 1052.5 J, 558.46 J, and 713.68 J. Their SEA values are 6.99 J/gr, 4.4 J/gr, and 7.14 J/gr, respectively (the errors between experimental and numerical

results of EA and SEA parameters for APA, APP, and PPP specimens are 6.84%-6.73%, 2.3%-0.1%, and 3.0%-0.92%, respectively).

Table 8

Figure 27

Finally, it can be concluded that high sensitivity of PP tubes to strain rate under low-velocity impact compression loading in PPP sandwich tube can improve the performance of this specimen compared to APA and APP; in this regard, PPP has the highest SEA, CFE, and CLE values under low-velocity impact loading. In contrast to the PPP sandwich tube results, the APP specimen did not show acceptable performance in impact loading compared to the observations in quasi-static loading. This specimen has the highest EA and SEA in quasi-static loading, but in impact loading, the mentioned parameters are lowest in this specimen.

The increase in PCF, MCF, EA, and SEA parameters in low-velocity impact loading to determine the strain rate effects on critical energy absorption parameters in sandwich tubes under two loading types, is shown in Figure 28, compared to quasi-static loading for a constant displacement. Due to the high sensitivity of sandwich tubes' components, especially PP tubes, to strain rate effects, the PCF, MCF, EA, and SEA parameters for three defined specimens increased significantly under low-velocity impact loading as compared with quasi-static compression loading. Among three specimens, the PPP sandwich tube has the highest increase in the mentioned parameters due to the more PP components than the two others. The PCF, MCF, EA, and SEA parameters in this specimen under low-velocity impact loading increased by 189.64%, 291.78%, 292.1%, and 277.96%, respectively, as compared with quasi-static compression loading. Furthermore, the lowest increase level occurred in APP despite having more PP components than APA. The reason for this can be the collapsing procedure of this specimen. This will be dealt with in the following section.

Figure 28

4.3.2   Low-velocity post-crushing morphologies of bio-inspired hybrid sandwich tubes:

According to the collapsing of APA specimen in experimental and numerical models (shown in Figure 29), it can be noted that in the external Al tube, the folding process has started from top to the bottom in non-axisymmetric diamond mode (Diamond 4-lobe) with four circumferential corners (N=4) and regular sides. By comparing the folding patterns of this tube with the similar specimen under quasi-static compression, it can be seen that the concertina mode

in this tube under quasi-static compression has changed into a non-axisymmetric diamond mode (Diamond 4-lobe) under low-velocity impact loading. Therefore, it can be concluded that the effects of strain rate on folding modes of this tube are negative compared with the one in quasi-static loading. On the other hand, an examination of the collapse mechanism for the internal tube in this specimen shows that this tube, in contrast to the external tube, started its folding process from the end, and the folding mode did not change compared to a similar specimen under quasi-static loading. It is formed in non-axisymmetric diamond mode (Diamond 4-lobe). Moreover, based on Figure 29, some core tubes underwent longitudinal cracking. Also, comparing the experimental and numerical collapsed specimens shows that the numerical model could correctly predict the number and shape of external and internal tube folds.

Figure 29

By examining the collapsing mechanisms of APP specimen under low-velocity impact loading (shown in Figure 30), it can be noted that in contrast to APA specimen, the folding for all components of this sandwich tube has started from the end. This specimen's folding mode of two Al and PP tubes is in Diamond 3-lobe with three circumferential corners (N=3). By comparing the folds in tubes of this specimen under both loading, it can be deduced that despite the similarity of the shape of the first fold of the internal tube under quasi-static and low-velocity impact loadings, this tube has cracked significantly at the middle section under low-velocity impact loading. Moreover, the folding mode of the external Al tube has changed from non-axisymmetric diamond mode (Diamond 4-lobe) in quasi-static loading to non-axisymmetric diamond mode (Diamond 3-lobe) under low-velocity impact loading. On the other hand, it is observed that components of this sandwich tube go through a significant amount of cracks under low-velocity impact loading, and strain rate has negative effects on their folding mode compared with two other specimens. Hence, the APP specimen under low-velocity impact loading has the worst performance among the three sandwich tubes. As proposed in Figure 28, the increase in PCF, MCF, EA, and SEA parameters is the lowest in this specimen compared to the two other specimens and quasi-static loading. According to Figure 30(a) and (b), there is a proper agreement between collapsed experimental and numerical models as for the APP specimen.

Figure 30

Similar to the APP, folding of all PPP specimen components under low-velocity impact loading, as shown in Figure 31, has started from its end. The first fold of the external PP tube from the end is in concertina mode. This fold is in non-axisymmetric diamond mode (Diamond 3-lobe) in the external tube of PPP under quasi-static loading. Also,

circumferential and longitudinal cracks are seen due to the impact effects on some core and internal tubes. The presence of cracks at the middle section of the internal tube in PPP prevents the folding process in this tube during crushing. In this specimen, despite the unknown behavior of PP tubes under axial low-velocity impact loading, the defined numerical model could successfully predict crushing mechanisms.

Observing the crushing mechanisms of collapsed models in all three specimens determined that cracks are formed in most PP components. This can be due to the interaction between sandwich tube components and top and bottom plates resulting from impact and temperature effects; Polypropylene tubes have a brittle behavior in the low-temperature range under impact loading [38]. Although the high deformable behavior of PP tubes causes a reduction in their energy absorption, the cracking issue can be solved by raising the temperature above room temperature.

Figure 31

In the end, results from the trend of force-displacement curves, critical energy absorption parameters, and experimental and numerical models of crushing mechanisms for sandwich tubes under low-velocity impact compression loading showed that the numerical model could, to an acceptable extent, predict the crushing behavior of experimented specimens. As mentioned in section 3.3.1, for simulation of PP tubes in strain rate from low-velocity impact compression loading, the elastic modulus, and yield stress should be increased by 10% and 30%, respectively, as compared with their values under quasi-static compression [37]. Moreover, according to [61, 62], the aluminum material has a limited sensitivity to strain rate at the range of $[10^{-4}\text{-}10^3]$ ($1/_s$), and the mechanical properties used in quasi-static loading can be employed during simulation under low-velocity impact loading.

4.3.3   *Effects of designing parameters on low-velocity impact response:*

After simulation of sandwich tubes under low-velocity impact loading and examining the obtained results, it is determined that a numerical model could well predict the behavior of specimens under this loading. After correcting the numerical simulation, similar to the numerical study in the quasi-static loading, three structures presented in Table 6 and Figure 21, are studied under axial low-velocity impact loading. Similar to experimental specimens under low-velocity impact loading, all defined sandwich tubes with the kinetic energy of 1057.86 J and similar boundary conditions to experimental specimens collapsed. To understand the efficiency and energy absorption of specimens

under low-velocity impact loading, in addition to the force-displacement curve, the results of critical energy absorption parameters, including PCF, MCF, EA, SEA, CFE, and CLE, are proposed for each sandwich tube.

By comparing the force-displacement curves in Figure 32(a), (b), and (c), it can be noted that the material of hollow core tubes is highly effective on energy absorption parameters and fluctuations of force-displacement curves, just as the numerical study of sandwich tubes under quasi-static loading. The fluctuation and slope of the force-displacement curve in the elastic region for most specimens with Al cores and each of three defined configurations are higher than specimens with PP cores with a similar configuration.

Comparing the force-displacement curves (shown in Figure 32) and results of

Table *9*, for sandwich tubes with the same component material and different configurations, it can be concluded that sandwiching hollow tubes in configuration 3 are similar quasi-static loading, gives the highest PCF and MCF. On the other hand, the lowest value in two parameters is obtained for each specimen in configuration 1. However, the results of Figure 32(d) show that sandwiching hollow tubes with each desired material permutation in configuration 1 gives the highest SEA value in contrast to results obtained under quasi-static loading. Therefore, although defined specimens in configuration 1 have a lower MCF and PCF value, the defined specimens with a lower weight than specimens with similar material in two other configurations absorb the entire imposed energy with a higher crushing length. On the other hand, sandwiching hollow tubes in configuration 3, even though it increases PCF and MCF values, gives the lowest SEA and CLE under imposed kinetic energy. Also, the results of the EA parameter in sandwich tubes with Al cores (shown in Figure 32(d)) indicate that sandwiching hollow tubes in configurations 2, 1, and 3, respectively, gives the highest energy absorptions. However, specimens with PP cores, including APP and APA, experienced the lowest EA value in configuration 2 compared with two other configurations. On the other hand, although the MCF and PCF values are lower in PPP in configurations 1 and 2 than in configuration 3, the higher crushing length of this specimen equated energy absorption EA for this specimen in all three configurations to 689.17 J.

On the other hand, investigation of EA and SEA parameters in sandwich tubes with a similar configuration show that in the specimen in configuration 1, even although two PAA and PAP specimens have the highest EA value as in quasi-static loading, sandwich tubes with PP tubes (APP and APA) have the highest SEA value due to the higher PP

component that is affected by strain rates in low-velocity impact loading; in this configuration, PAA and PAP specimens have the largest EA value. Also, despite that, the highest EA value belongs to AAA and AAP with configuration 2, PPP and APA have the largest SEA value, respectively, and a lower EA value than specimens with Al core. Between specimens of configuration 3, APP and APA have the largest EA and SEA values, respectively, in contrast to quasi-static loading. Observing parameters of table 9 shows that between specimens with configurations 1 and 3, AAA sandwich tube with Al cores has the lowest crushing length and largest CFE, PCF, and MCF values. Furthermore, this specimen achieved the largest CFE and PCF values in configuration 2 among specimens with a similar configuration.

   As mentioned, sandwiching APP tube components in configurations 1 and 3 caused a desirable efficiency and highest SEA value in specimens with a similar configuration. Due to destructive interaction effects in configuration 2, this specimen has the lowest EA and SEA among sandwich tubes with a similar configuration. Finally, specimens with the largest SEA value in each configuration are shown in Figure 33, according to the results, APP specimens in configurations 1 and 3 and PPP specimens in configuration 2 have the largest SEA value compared to specimens with similar configurations.

<div align="center">Figure 32</div>

<div align="center">Table 9</div>

<div align="center">Figure 33</div>

4.3.4   Interaction effect between sandwich tube components under low-velocity impact:

   As in section 4.2.4, the effects of interaction between the components of the sandwich tubes under quasi-static compression were investigated. This section also examine this issue for the samples defined in the numerical study (shown in Figure 21) is treated under the low-velocity impact loading. For this purpose, all single hollow aluminum and polypropylene tubes used in sandwich tubes with the same kinetic energy and boundary conditions as the bio-inspired specimens defined in section 4.3, under low-velocity impact loading, have been numerically simulated. A comparison was made between the values of PCF, MCF, CFE, EA, and SEA parameters for each sandwich tube and the sum of their components to investigate the interaction effects between the sample components. It is observed that the specimens with the external aluminum tube except for the APA sample in Configurations 1 and 2 have been able

to reduce the amount of PCF relative to the sum of the value of this parameter in the respective components when Examining the amount of changes in the mentioned parameters for each sandwich tube with the sum of their components in all three configurations (shown in Figure 34). On the other hand, sandwiching single hollow tubes in all specimens in configuration 3 has increased the amount of peak force in the sandwich tube relative to the sum of this parameter in the components. Also, the sandwich tubes defined as configuration 3 had the largest increase in MCF, EA, and SEA parameters relative to the sum associated with their components.

It can be concluded that the material of the core tubes is very influential in the results considering the results obtained for samples with different material permutations and the same configuration. As can be seen in the specimens with configuration 1, by changing the material of the core tubes from aluminum to polypropylene, the amount of peak force increases relative to the sum of this parameter in the relevant components. This trend is also observed in the specimens defined in configuration 3. On the other hand, in most samples of all three configurations, the amount of CFE has increased in relation whit the sum of the relevant components by replacing the aluminum core tubes instead of the polypropylene core tubes. Also, by comparing the results presented in the samples with the same configuration (shown in Figure 34(b)), it is observed that the increase of EA in AAA-AAP specimens and also the increase of SEA in PPA-PPP samples compared to the sum of components had the lowest and highest values, respectively. Finally, it can be concluded that sandwiching single hollow tubes as hierarchical structures defined in all specimens under low-velocity impact loading increases the value of MCF, CFE, EA and SEA relative to the sum of each parameter in the components of each sandwich tube. Also, sandwiching single hollow tubes in all samples except AAA, AAP, APP defined in configuration 2, and APA in configuration 1 has increased the value of the PCF parameter compared to the sum of this parameter in the relevant components. Therefore, from this point of view, sandwiching single hollow tubes has not had a good effect.

Figure 34

4.3.5   *Comparison of low-velocity to quasi-static variations of crush parameters:*

As mentioned in section 3.3.1, for simulation of Al tubes under low-velocity impact loading in strain rate range of $[10^{-4}\text{-}10^{3}]$ (1/S), they are insignificantly affected by strain rate. However, contrary to these tubes, the behavior of PP tubes is a function of strain rate. For further understanding of the effects of low-velocity impact loading and strain rate

on components of sandwich tubes, especially PP tubes, the critical energy absorption parameters (PCF, MCF, EA, and SEA) for sandwich tubes under two loading types of low-velocity impact and quasi-static are compared at similar displacements. This comparison is performed for all sandwich tubes defined in numerical modeling.

By studying the critical energy absorption parameters from force-displacement curves, it is noted that PCF, MCF, EA, and SEA parameters increased in all defined specimens under low-velocity impact loading compared with quasi-static loading (shown in Figure 35(a), (b)). The results of mentioned parameters for sandwich tubes with a similar configuration demonstrate that specimens with PP cores (PPP-PPA-APP-APA) exhibit the most significant increase under low-velocity impact loading than under quasi-static loading, contrary to sandwich tubes with Al cores (PAP-PAA-AAP-AAA).

By examining the specimens with the same material but different configurations, it is noted that sandwiching most specimens in configuration 3, due to larger number of core tubes and an internal tube with a larger diameter, caused the most significant increase in PCF, MCF, EA, and SEA parameters under low-velocity impact loading than in quasi-static loading. Hence, as the number of cores increases from configuration 1 to configuration 3, changes in mentioned parameters under low-velocity impact loading become more significant than quasi-static loading. However, in some sandwich tubes, such as APA specimen, the highest increase for mentioned parameters occurred in configuration 2 and sandwiching PPP specimen in configurations 1, 2, and 3 led to the most significant increase in three MCF, EA, and SEA parameters, respectively, under low-velocity impact loading.

Finally, based on MCF, EA, and SEA parameters, it can be argued that strain rate effects in low-velocity impact loading on PPP sandwich tubes' components in configurations 1 and 2 and on PPA specimen in configuration 3 made these sandwich tubes known as having the best performance under low-velocity impact loading than quasi-static loading. Moreover, from an energy absorption point of view, with the most significant increase in PCF parameter, sandwich tubes AAA and AAP have the least significant increase among eight defined specimens with configurations 1 and 3. Also, between specimens in configuration 2, AAA and PAA sandwich tubes have the lowest increase in PCF parameters, respectively.

Figure 35

5.   Conclusion

This research aims to investigate the behavior of pure polypropylene pipes along whit aluminum tubes with regard to folding capability, sensitivity to strain rate, ease of construction and deformation, renewable, good mechanical properties compare to low weight, and low cost, as well as the effects hierarchical structure by generating appropriate interaction is done. To do this, we examined full-PP and Al/PP second-order hierarchical structures inspired by horsetail, human tendons, and spongy bone, a promising approach for designing novel combined-material hierarchical structures experimentally and numerically. Also, the effect of materials used for internal, external, and core tubes in a given geometry was evaluated experimentally and numerically. In the numerical investigation of the effect of the internal and the core tubes' diameter, two other geometries were considered in addition to experimental ones. In all three geometries, the effect of tube material was examined by a complete factorial approach. The concluded remarks are as follows:

1- Comparing the collapse mechanisms of single hollow Al and PP tubes with sandwich tubes under quasi-static loading shows that hierarchical structure improves the collapse mechanisms of single hollow tubes. This includes external Al tube in APP and APA and external and internal PP tubes in PPP and internal PP tube in APP.

2- Sandwich tubular structures increase loading capacity and energy absorption under quasi-static loading compared to single hollow tubes. Also, comparing the results between three APP, APA, and PPP specimens reveals that the highest PCF, MCF, EA, and SEA values are for APP, despite fewer Al components relative to APA. Also, under low-velocity impact loading, despite that, the EA of APA is the highest and SEA of PPP specimens are almost the same. Moreover, PPP is more cost-efficient and has more convenient renewability.

3- The numerical results of PCF, MCF, EA, and SEA parameters for each specimen under two loading conditions show that the parameters increase significantly under low-velocity impact loading compared to quasi-static loading. This may be due to the high sensitivity of PP tubes to the strain rate. As the number of PP components increases in specimens, this difference in the four mentioned parameters is increasingly highlighted. For instance, in PPP, the PCF, MCF, EA, and SEA values have increased by 163.31%, 263.91%, 294.68%, and 293.71%, respectively, under dynamic loading relative to quasi-static loading that indicates better performance and higher efficiency of PPP under this loading.

4- Based on numerical results under quasi-static loading for three defined configurations, the highest EAs among specimens of configurations 1, 2, and 3 are for sandwich tubes PAA (1792.18 J), AAA (3229.94 J), and AAA (4976.42 J), respectively. Also, the largest SEA values are for specimens PAP (12.83 J/g), PAA (13.86 J/g), and AAA (20.13 J/g), respectively. On the other hand, by comparing the results of low-velocity impact loading, it can be concluded that the highest EAs are for sandwich tubes PAP (1089.0 J), AAA (1123.25 J), and APP (1082.46 J), respectively. Also, the largest SEAs are for specimens APP (9.34 J/g), PPP (6.89 J/g), and APP (7.04 J/g), respectively.

5- Considering the interaction effects between the sandwich tube components, it can be seen that sandwiching single hollow tubes significantly increases (especially the specimens defined as configuration 3), MCF, EA, SEA, and CFE in most specimens when compared to the sum of these parameters in their single hollow tubes. Furthermore, sandwiching single tubes under quasi-static loading considerably decreases the peak force compared to the sum of this parameter in each specimen's components (especially the specimens defined as configuration 1).

References

[1] M. Moeinifard, G. Liaghat, G. Rahimi, A. Talezadehlari, H. Hadavinia, Experimental investigation on the energy absorption and contact force of unstiffened and grid-stiffened composite cylindrical shells under lateral compression, Composite Structures 152 (2016) 626-636.
[2] R. Eshkoor, S. Oshkovr, A. Sulong, R. Zulkifli, A. Ariffin, C. Azhari, Effect of trigger configuration on the crashworthiness characteristics of natural silk epoxy composite tubes, Composites Part B: Engineering 55 (2013) 5-10.
[3] C. Kılıçaslan, M. Güden, İ.K. Odacı, A. Taşdemirci, Experimental and numerical studies on the quasi-static and dynamic crushing responses of multi-layer trapezoidal aluminum corrugated sandwiches, Thin-Walled Structures 78 (2014) 70-78.
[4] N. San Ha, G. Lu, A review of recent research on bio-inspired structures and materials for energy absorption applications, Composites Part B: Engineering 181 (2020) 107496.
[5] H. Han, F. Taheri, N. Pegg, Quasi-static and dynamic crushing behaviors of aluminum and steel tubes with a cutout, Thin-walled structures 45(3) (2007) 283-300.
[6] X. Sun, H. Zhang, W. Meng, R. Zhang, K. Li, T. Peng, Primary resonance analysis and vibration suppression for the harmonically excited nonlinear suspension system using a pair of symmetric viscoelastic buffers, Nonlinear Dynamics 94(2) (2018) 1243-1265.
[7] R.-H. Zhang, Z.-C. He, H.-W. Wang, F. You, K.-N. Li, Study on self-tuning tyre friction control for developing main-servo loop integrated chassis control system, Ieee Access 5 (2017) 6649-6660.
[8] Y. Zhang, Q. Liu, Z. He, Z. Zong, J. Fang, Dynamic impact response of aluminum honeycombs filled with Expanded Polypropylene foam, Composites Part B: Engineering 156 (2019) 17-27.
[9] C. Reuter, K.-H. Sauerland, T. Tröster, Experimental and numerical crushing analysis of circular CFRP tubes under axial impact loading, Composite Structures 174 (2017) 33-44.
[10] K. Vinayagar, A.S. Kumar, Crashworthiness analysis of double section bi-tubular thin-walled structures, Thin-Walled Structures 112 (2017) 184-193.
[11] A. Tarafdar, O. Razmkhah, H. Ahmadi, G. Liaghat, S. Chitsaz Charandabi, M. Rezaei Faraz, Effect of layering layout on the energy absorbance of bamboo-inspired tubular composites, Journal of Reinforced Plastics and Composites (2022) 07316844211063865.
[12] A. Abosbaia, E. Mahdi, A. Hamouda, B. Sahari, A. Mokhtar, Energy absorption capability of laterally loaded segmented composite tubes, Composite structures 70(3) (2005) 356-373.
[13] S. Ochelski, P. Gotowicki, Experimental assessment of energy absorption capability of carbon-epoxy and glass-epoxy composites, Composite Structures 87(3) (2009) 215-224.

[14] J. Fu, Q. Liu, K. Liufu, Y. Deng, J. Fang, Q. Li, Design of bionic-bamboo thin-walled structures for energy absorption, Thin-Walled Structures 135 (2019) 400-413.

[15] S. Taghizadeh, A. Farrokhabadi, G. Liaghat, E. Pedram, H. Malekinejad, S.F. Mohammadi, H. Ahmadi, Characterization of compressive behavior of PVC foam infilled composite sandwich panels with different corrugated core shapes, Thin-Walled Structures 135 (2019) 160-172.

[16] A. Tarafdar, G. Liaghat, H. Ahmadi, O. Razmkhah, S.C. Charandabi, M.R. Faraz, E. Pedram, Quasi-static and low-velocity impact behavior of the bio-inspired hybrid Al/GFRP sandwich tube with hierarchical core: Experimental and numerical investigation, Composite Structures 276 (2021) 114567.

[17] A. Mamalis, D. Manolakos, G. Demosthenous, W. Johnson, Axial plastic collapse of thin bi-material tubes as energy dissipating systems, International Journal of Impact Engineering 11(2) (1991) 185-196.

[18] A. Niknejad, M.M. Abedi, G.H. Liaghat, M.Z. Nejad, Prediction of the mean folding force during the axial compression in foam-filled grooved tubes by theoretical analysis, Materials & Design 37 (2012) 144-151.

[19] S. Xie, W. Yang, N. Wang, H. Li, Crashworthiness analysis of multi-cell square tubes under axial loads, International Journal of Mechanical Sciences 121 (2017) 106-118.

[20] X. Xu, Y. Zhang, J. Wang, F. Jiang, C.H. Wang, Crashworthiness design of novel hierarchical hexagonal columns, Composite Structures 194 (2018) 36-48.

[21] R. Kalhor, H. Akbarshahi, S.W. Case, Numerical modeling of the effects of FRP thickness and stacking sequence on energy absorption of metal–FRP square tubes, Composite Structures 147 (2016) 231-246.

[22] S.P. Santosa, T. Wierzbicki, A.G. Hanssen, M. Langseth, Experimental and numerical studies of foam-filled sections, International journal of impact engineering 24(5) (2000) 509-534.

[23] A. Niknejad, S.A. Elahi, G.H. Liaghat, Experimental investigation on the lateral compression in the foam-filled circular tubes, Materials & Design (1980-2015) 36 (2012) 24-34.

[24] A. Niknejad, B. Rezaei, G.H. Liaghat, Empty circular metal tubes in the splitting process–theoretical and experimental studies, Thin-walled structures 72 (2013) 48-60.

[25] B. Rezaei, A. Niknejad, H. Assaee, G.H. Liaghat, Axial splitting of empty and foam-filled circular composite tubes — An experimental study, Archives of Civil and Mechanical Engineering 15 (2015) 650.

[26] J. Bouchet, E. Jacquelin, P. Hamelin, Dynamic axial crushing of combined composite aluminium tube: the role of both reinforcement and surface treatments, Composite structures 56(1) (2002) 87-96.

[27] F. Xu, Enhancing material efficiency of energy absorbers through graded thickness structures, Thin-Walled Structures 97 (2015) 250-265.

[28] I. Duarte, L. Krstulović-Opara, M. Vesenjak, Axial crush behaviour of the aluminium alloy in-situ foam filled tubes with very low wall thickness, Composite Structures 192 (2018) 184-192.

[29] Y. Xiang, T. Yu, L. Yang, Comparative analysis of energy absorption capacity of polygonal tubes, multi-cell tubes and honeycombs by utilizing key performance indicators, Materials & Design 89 (2016) 689-696.

[30] M. Polanco-Loria, A.H. Clausen, T. Berstad, O.S. Hopperstad, Constitutive model for thermoplastics with structural applications, International Journal of Impact Engineering 37(12) (2010) 1207-1219.

[31] X. Castello, S. Estefen, Limit strength and reeling effects of sandwich pipes with bonded layers, International journal of mechanical sciences 49(5) (2007) 577-588.

[32] A. Güllü, A. Özdemir, E. Özdemir, Experimental investigation of the effect of glass fibres on the mechanical properties of polypropylene (PP) and polyamide 6 (PA6) plastics, Materials & design 27(4) (2006) 316-323.

[33] A.F. Wilde, R.W. Matton, J.M. Rogers, S.E. Wentworth, Effects of moisture on the high-speed impact response of selected polyurethane–polyether block copolymers, Journal of Applied Polymer Science 25(4) (1980) 615-625.

[34] E. Araújo, E. Hage Jr, A. Carvalho, Effect of compatibilizer in acrylonitrile-butadiene-styrene toughened nylon 6 blends: Ductile–brittle transition temperature, Journal of applied polymer science 90(10) (2003) 2643-2647.

[35] J. Ingram, Y. Zhou, S. Jeelani, T. Lacy, M.F. Horstemeyer, Effect of strain rate on tensile behavior of polypropylene and carbon nanofiber filled polypropylene, Materials Science and Engineering: A 489(1-2) (2008) 99-106.

[36] A. Arriaga, R. Pagaldai, A.M. Zaldua, A. Chrysostomou, M. O'Brien, Impact testing and simulation of a polypropylene component. Correlation with strain rate sensitive constitutive models in ANSYS and LS-DYNA, Polymer Testing 29(2) (2010) 170-180.

[37] M.M. Shokrieh, V.A. Joneidi, R. Mosalmani, Characterization and simulation of tensile behavior of graphene/polypropylene nanocomposites using a novel strain-rate-dependent micromechanics model, Journal of Thermoplastic Composite Materials 28(6) (2015) 818-834.

[38] M. Domaneschi, Experimental and numerical study of standard impact tests on polypropylene pipes with brittle behaviour, Proceedings of the Institution of Mechanical Engineers, Part B: Journal of Engineering Manufacture 226(12) (2012) 2035-2046.

[39] Q. Estrada, D. Szwedowicz, A. Rodriguez-Mendez, M. Elías-Espinosa, J. Silva-Aceves, J. Bedolla-Hernández, O.A. Gómez-Vargas, Effect of radial clearance and holes as crush initiators on the crashworthiness performance of bi-tubular profiles, Thin-Walled Structures 140 (2019) 43-59.

[40] C. Cui, Z. Wang, W. Zhou, Y. Wu, W. Wei, Branch point algorithm for structural irregularity determination of honeycomb, Composites Part B: Engineering 162 (2019) 323-330.

[41] H. El-Hage, P. Mallick, N. Zamani, A numerical study on the quasi-static axial crush characteristics of square aluminum–composite hybrid tubes, Composite structures 73(4) (2006) 505-514.

[42] J. Huang, X. Wang, Numerical and experimental investigations on the axial crushing response of composite tubes, Composite Structures 91(2) (2009) 222-228.

[43] A.A. Nia, J.H. Hamedani, Comparative analysis of energy absorption and deformations of thin walled tubes with various section geometries, Thin-Walled Structures 48(12) (2010) 946-954.

[44] L. Ying, T. Gao, W. Hou, M. Dai, X. Han, D. Jiang, On crashing behaviors of bio-inspired hybrid multi-cell Al/CFRP hierarchical tube under quasi-static loading: An experimental study, Composite Structures 257 (2021) 113103.

[45] K. Andrews, G. England, E. Ghani, Classification of the axial collapse of cylindrical tubes under quasi-static loading, International Journal of Mechanical Sciences 25(9-10) (1983) 687-696.

[46] S. Guillow, G. Lu, R. Grzebieta, Quasi-static axial compression of thin-walled circular aluminium tubes, International Journal of Mechanical Sciences 43(9) (2001) 2103-2123.

[47] L. Zhang, Z. Bai, F. Bai, Crashworthiness design for bio-inspired multi-cell tubes with quadrilateral, hexagonal and octagonal sections, Thin-Walled Structures 122 (2018) 42-51.

[48] A. Rahi, Controlling energy absorption capacity of combined bitubular tubes under axial loading, Thin-Walled Structures 123 (2018) 222-231.

[49] Q. Liu, X. Xu, J. Ma, J. Wang, Y. Shi, D. Hui, Lateral crushing and bending responses of CFRP square tube filled with aluminum honeycomb, Composites Part B: Engineering 118 (2017) 104-115.

[50] Q. Liu, Z. Mo, Y. Wu, J. Ma, G.C.P. Tsui, D. Hui, Crush response of CFRP square tube filled with aluminum honeycomb, Composites Part B: Engineering 98 (2016) 406-414.

[51] W. Chen, T. Wierzbicki, Relative merits of single-cell, multi-cell and foam-filled thin-walled structures in energy absorption, Thin-Walled Structures 39(4) (2001) 287-306.

[52] X. Zhang, G. Cheng, H. Zhang, Theoretical prediction and numerical simulation of multi-cell square thin-walled structures, Thin-Walled Structures 44(11) (2006) 1185-1191.

[53] H.-S. Kim, New extruded multi-cell aluminum profile for maximum crash energy absorption and weight efficiency, Thin-Walled Structures 40(4) (2002) 311-327.

[54] Z. Wang, J. Liu, Numerical and theoretical analysis of honeycomb structure filled with circular aluminum tubes subjected to axial compression, Composites Part B: Engineering 165 (2019) 626-635.

[55] W. Liu, Z. Lin, J. He, N. Wang, X. Deng, Crushing behavior and multi-objective optimization on the crashworthiness of sandwich structure with star-shaped tube in the center, Thin-Walled Structures 108 (2016) 205-214.

[56] Y. Xiao, H. Yin, H. Fang, G. Wen, Crashworthiness design of horsetail-bionic thin-walled structures under axial dynamic loading, International Journal of Mechanics and Materials in Design 12(4) (2016) 563-576.

[57] B. Chen, M. Zou, G. Liu, J. Song, H. Wang, Experimental study on energy absorption of bionic tubes inspired by bamboo structures under axial crushing, International Journal of Impact Engineering 115 (2018) 48-57.

[58] H. Tsang, S. Raza, Impact energy absorption of bio-inspired tubular sections with structural hierarchy, Composite Structures 195 (2018) 199-210.

[59] J. Hirsch, Recent development in aluminium for automotive applications, Transactions of Nonferrous Metals Society of China 24(7) (2014) 1995-2002.

[60] H. El-Hage, P. Mallick, N. Zamani, A numerical study on the quasi-static axial crush characteristics of square aluminum tubes with chamfering and other triggering mechanisms, International Journal of Crashworthiness 10(2) (2005) 183-196.

[61] S. Hsu, N. Jones, Quasi-static and dynamic axial crushing of thin-walled circular stainless steel, mild steel and aluminium alloy tubes, International journal of crashworthiness 9(2) (2004) 195-217.

[62] W. Abramowicz, N. Jones, Dynamic axial crushing of circular tubes, International Journal of Impact Engineering 2(3) (1984) 263-281.

Figures:
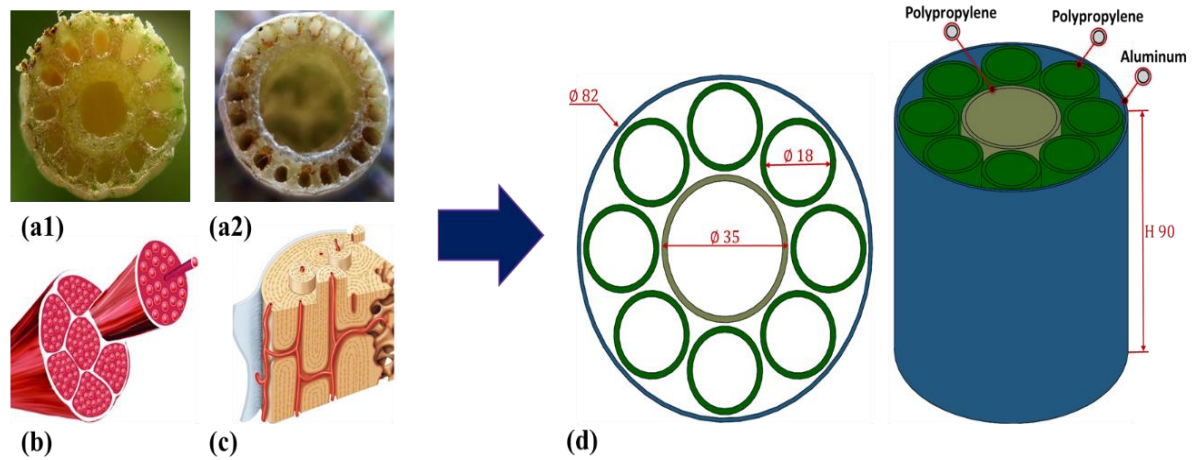
Figure 1 : Illustration of biological structures inspiriting bio-mimetic energy absorbers a) horsetail [56], b) human tendons [58], c) spongy bone [4], d) Schematic of a hybrid multi-cell sandwich tube (APP) [16].
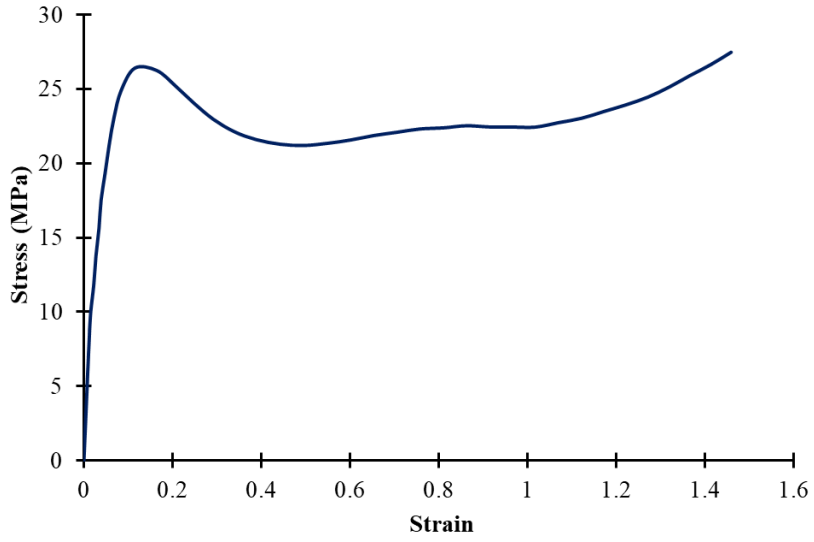
Figure 2 : Stress–strain curve of neat polypropylene under quasi-static loading.
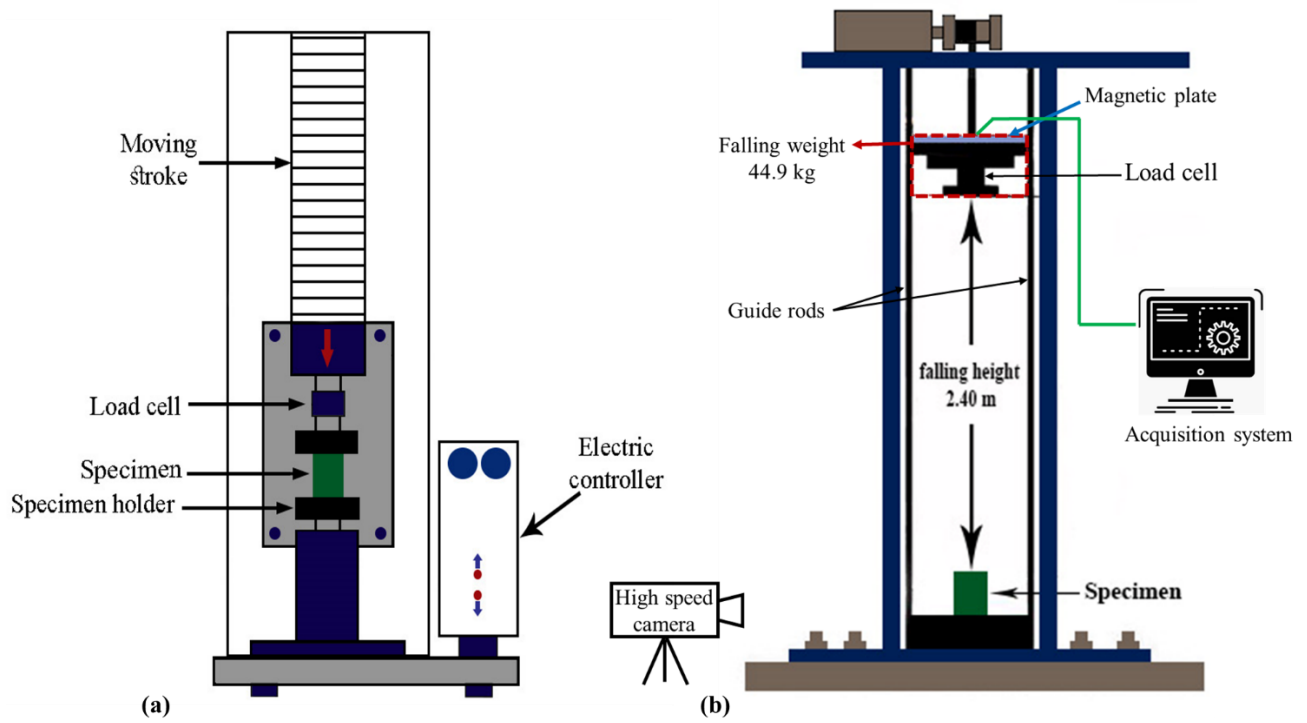
Figure 3 : Schematic of the (a) Quasi-static test setup and (b) Drop weight test setup.

(a1) 34 mm

(a2) 81 mm

(b1) 19.5 mm

(b2) 33.5 mm

(b3) 80.5 mm
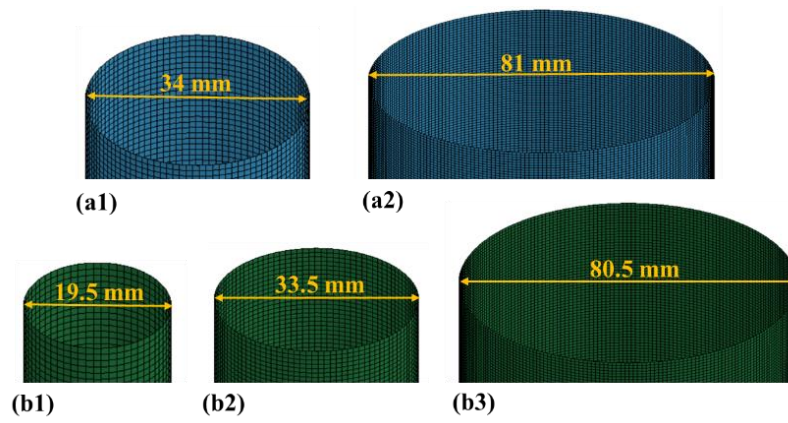
Figure 4: Simulated (a) aluminum tubes and (b) polypropylene tubes.

Internal PP

External Al

8 number Of cores

APP Specimen
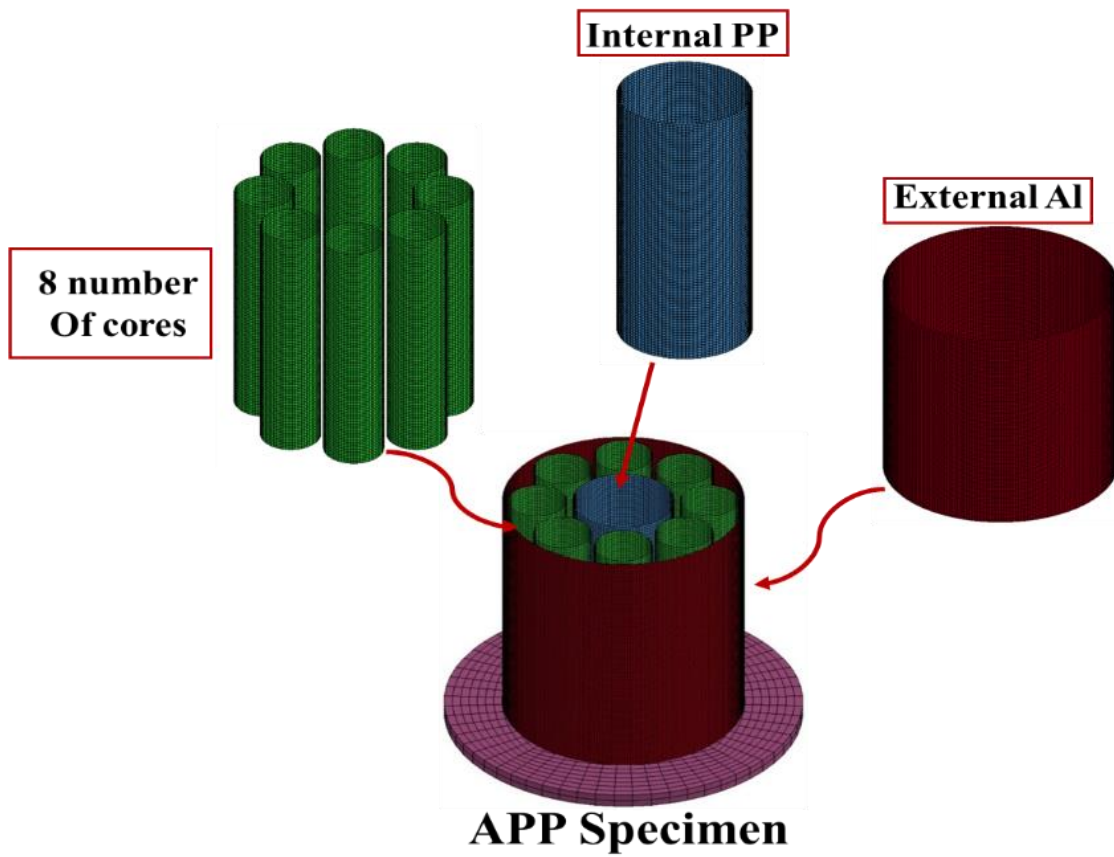
Figure 5: Simulation of the bio-inspired hybrid multi-cell sandwich tube (APP).
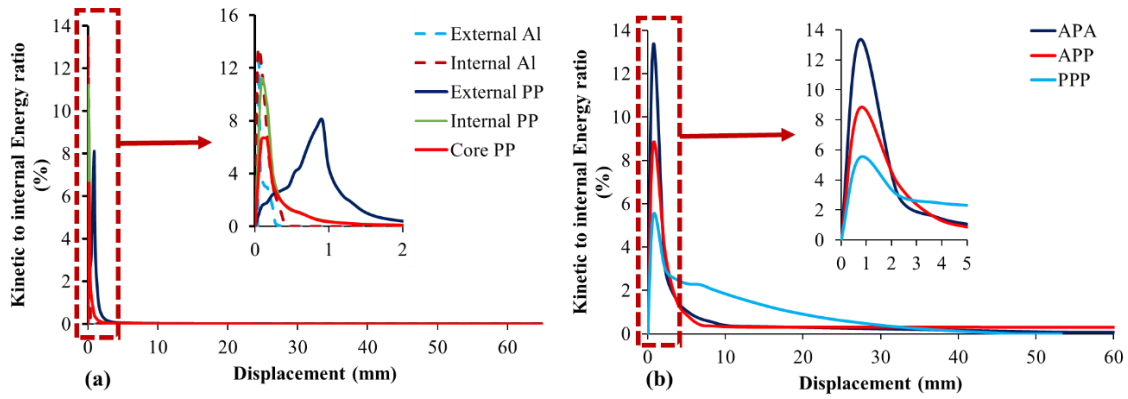
Figure 6: Ratio of the kinetic to internal energy versus displacement of (a) Single hollow tubes,

(b) Hybrid multi-cell sandwich tubes.
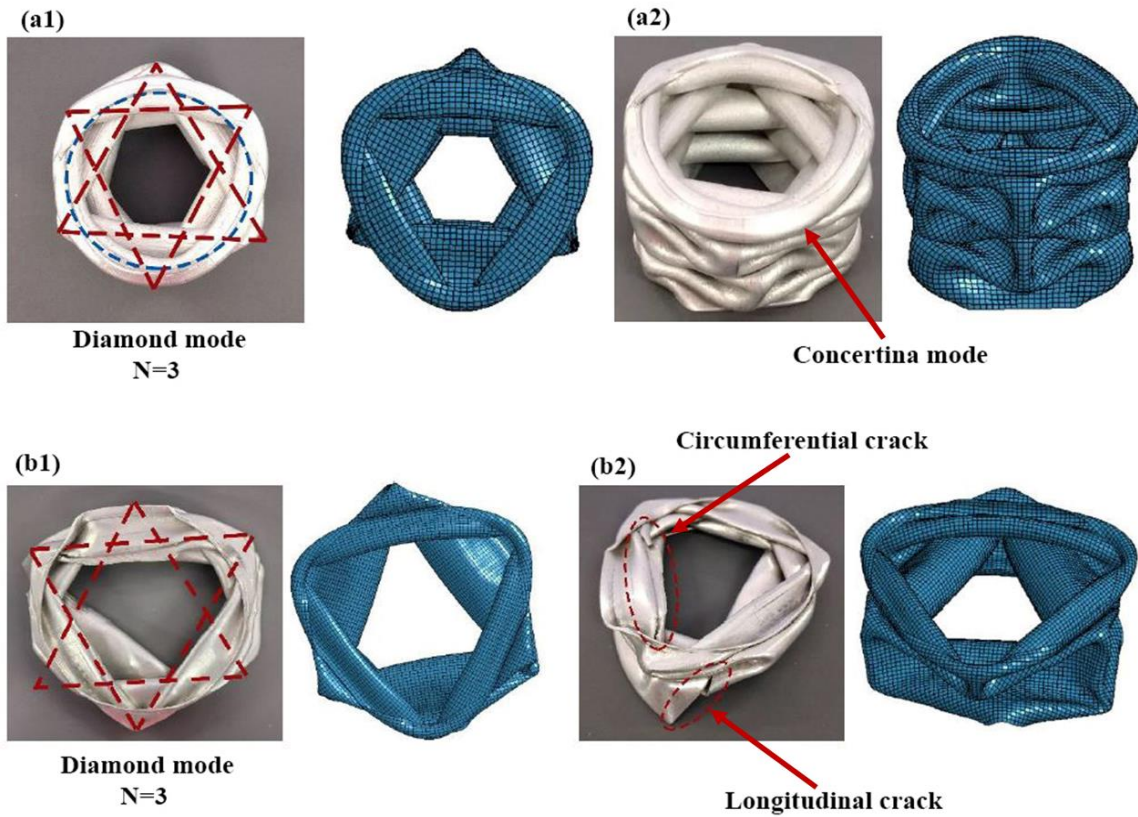
Figure 7: Comparison of axial crushing modes of Al tubes under axial crushing: (a) internal and, (b) external tube.
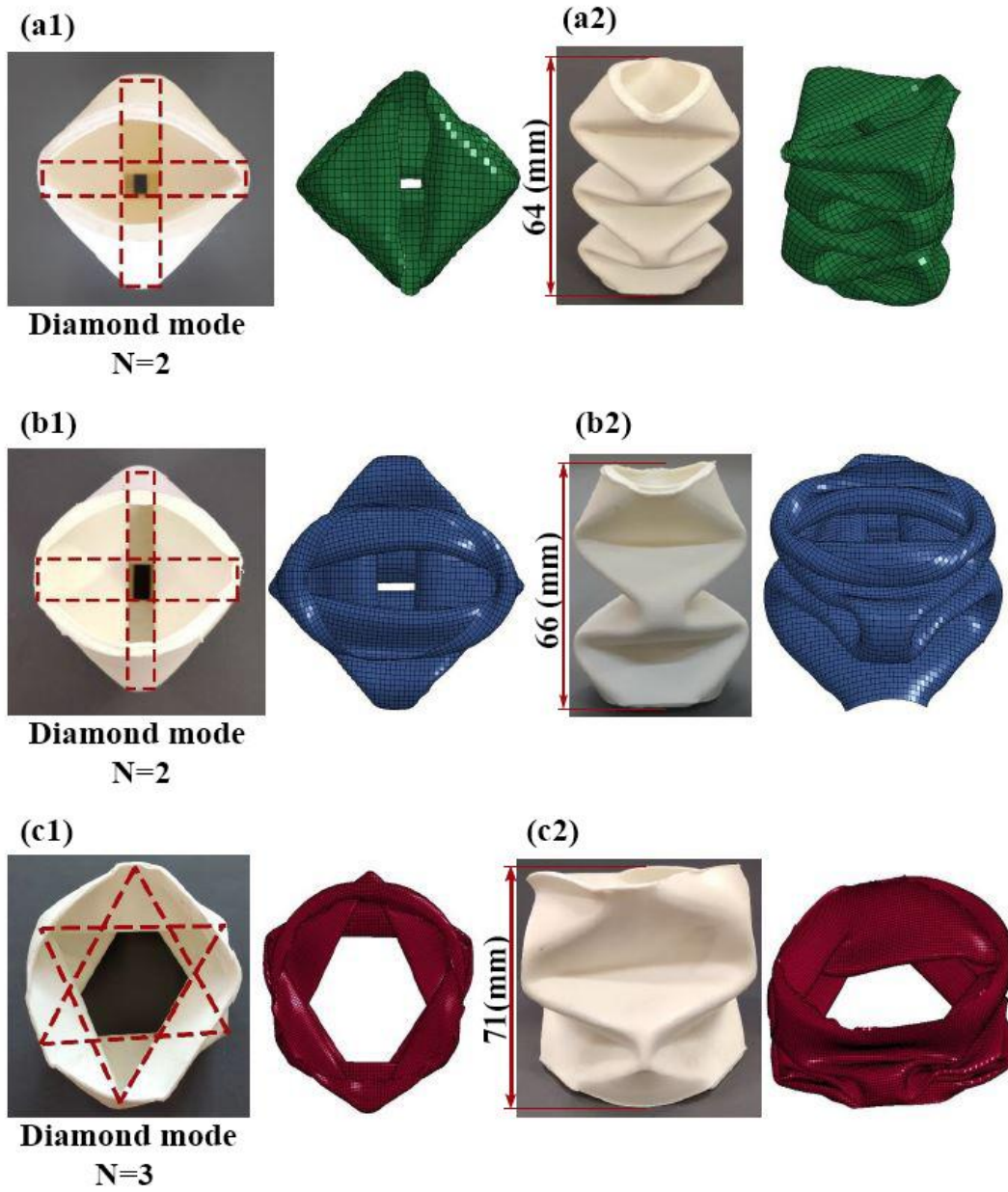
Figure 8: Comparison of axial crushing modes of PP tubes under axial crushing: (a) core, (b) internal, and (c) external tube.
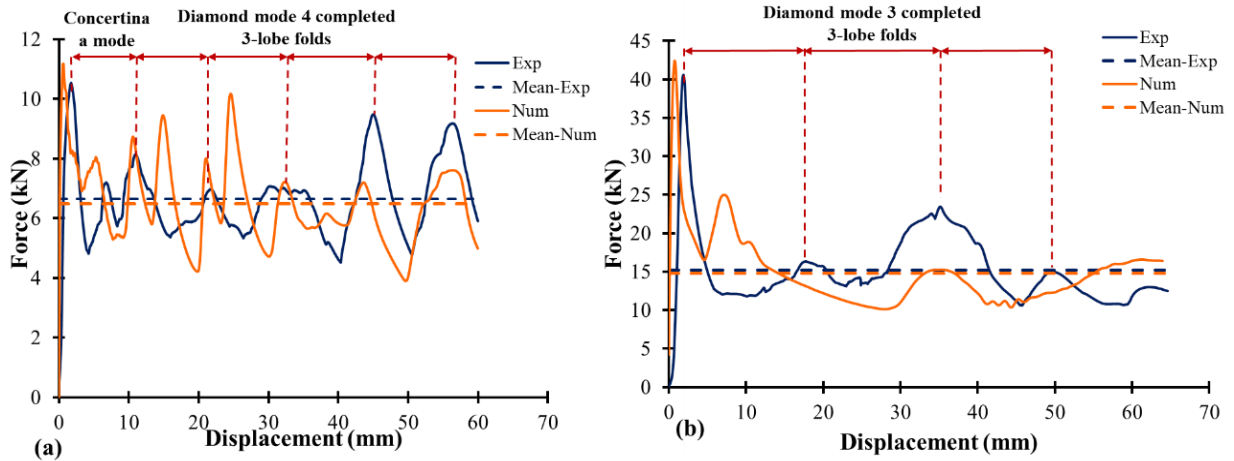
Figure 9: Force-displacement curves of Al tubes: (a) internal and (b) external.
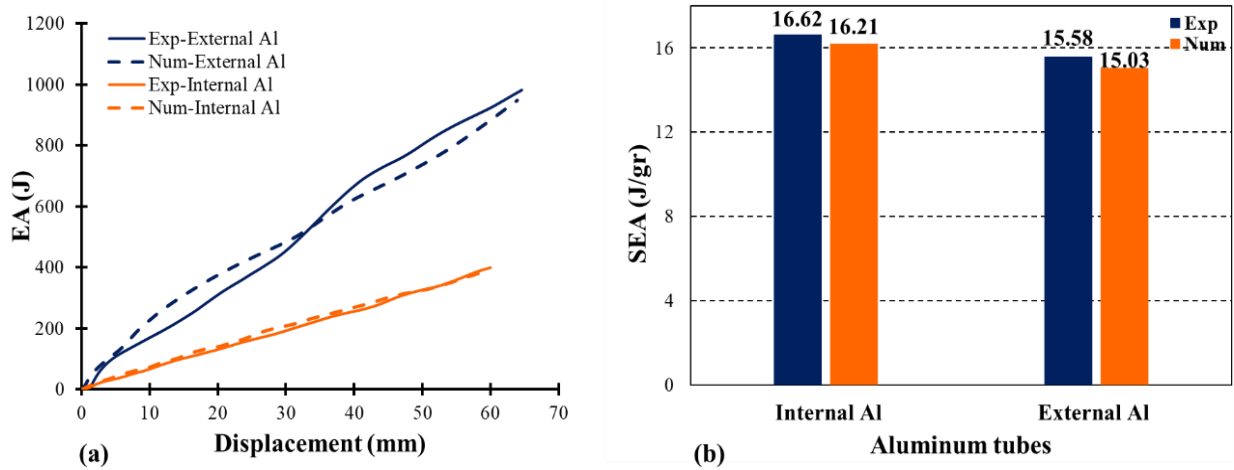
Figure 10: Comparison of (a) EA and, (b) SEA of individual hollow Al tubes.
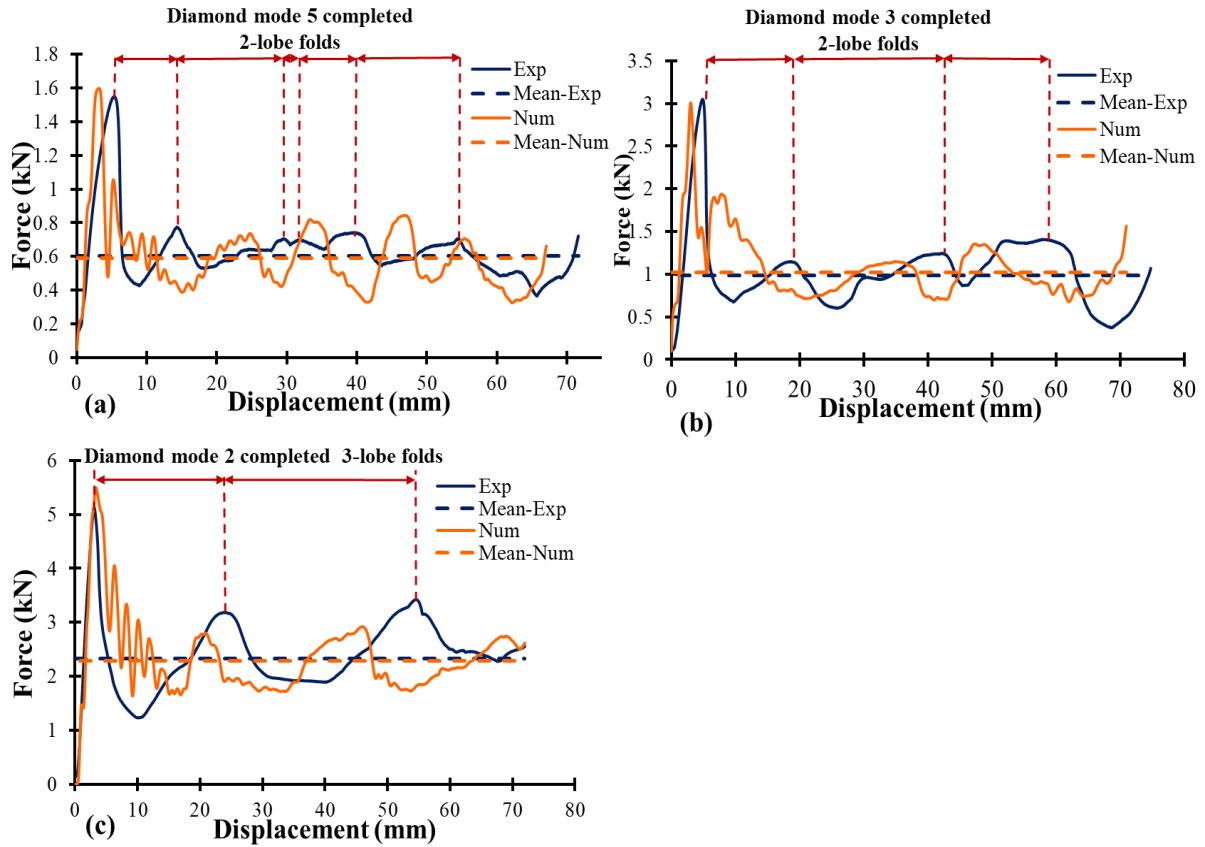
Figure 11: Force-displacement curves of PP tubes: (a) core, (b) internal, and (c) external.
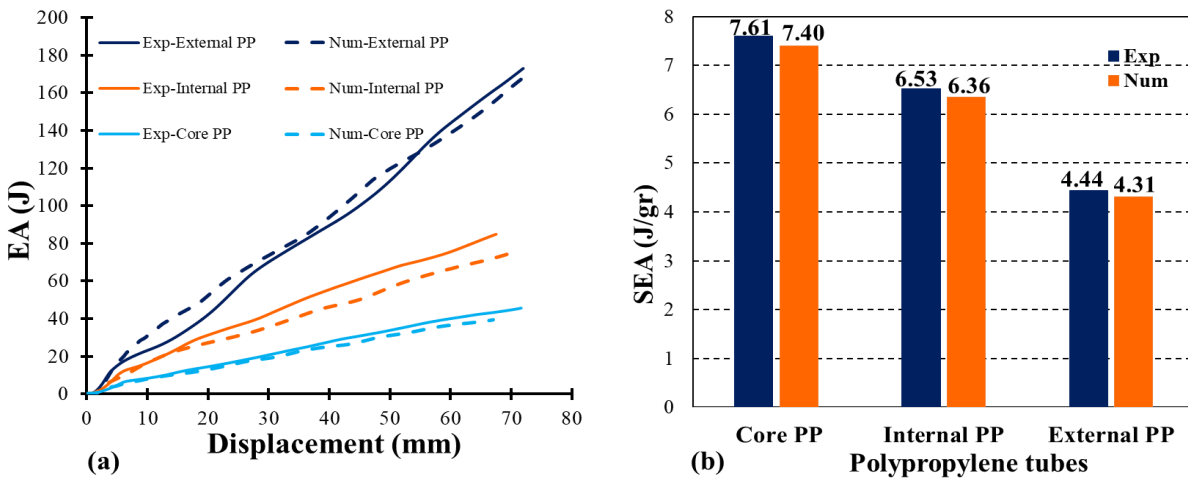
Figure 12: Comparison of (a) EA and, (b) SEA of individual hollow PP tubes.
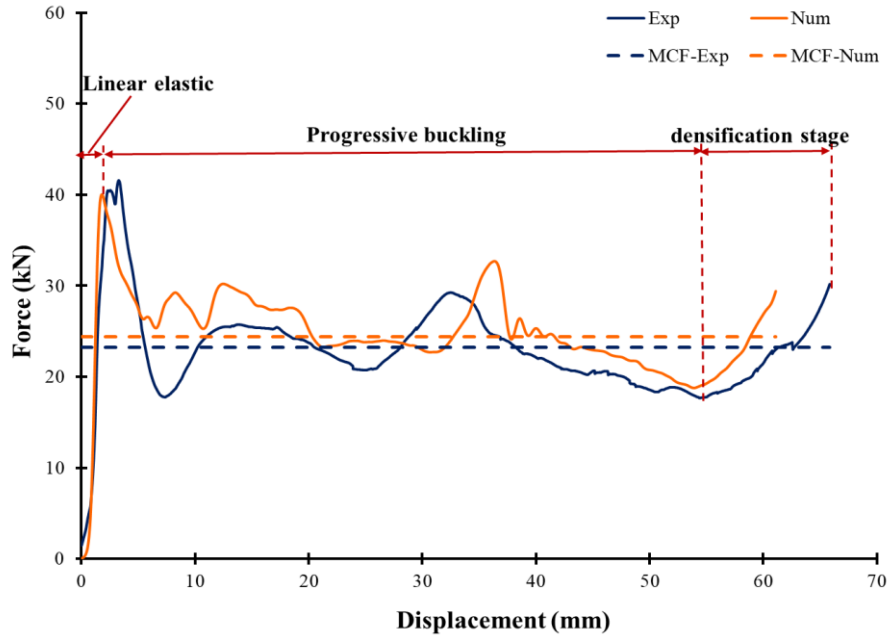
Figure 13: Force-displacement curves of APA specimen under quasi-static loading.
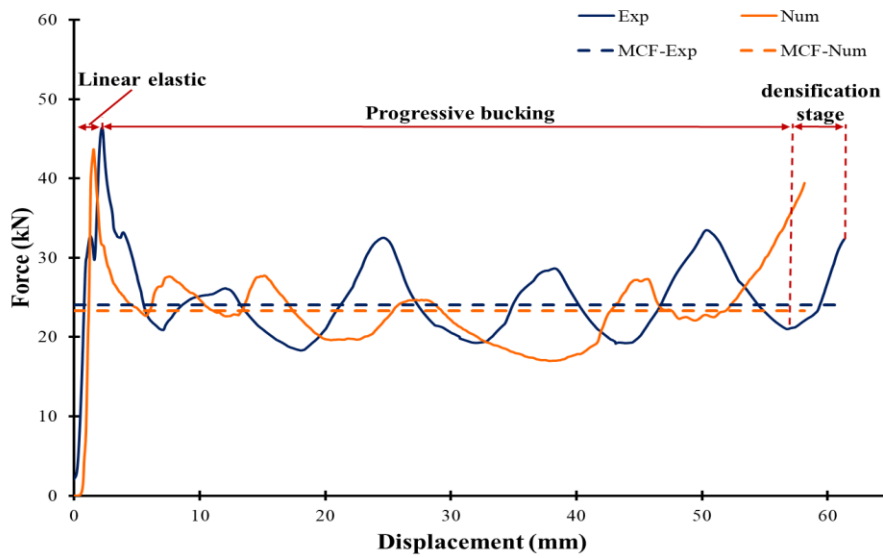
Figure 14: Force-displacement curves of APP specimen under quasi-static loading.
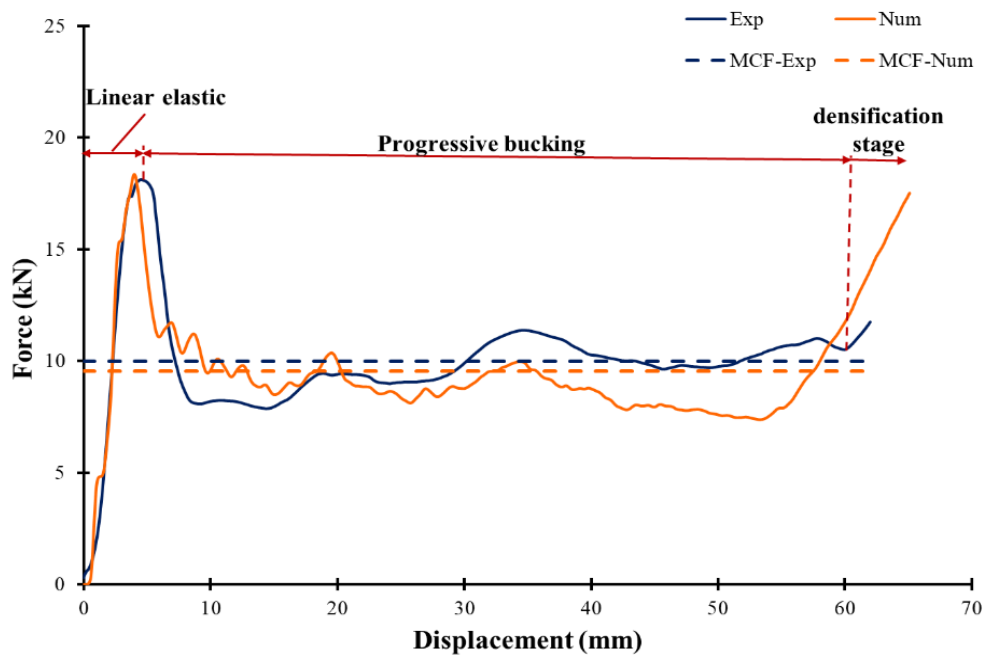
Figure 15: Force-displacement curves of PPP specimen under quasi-static loading.
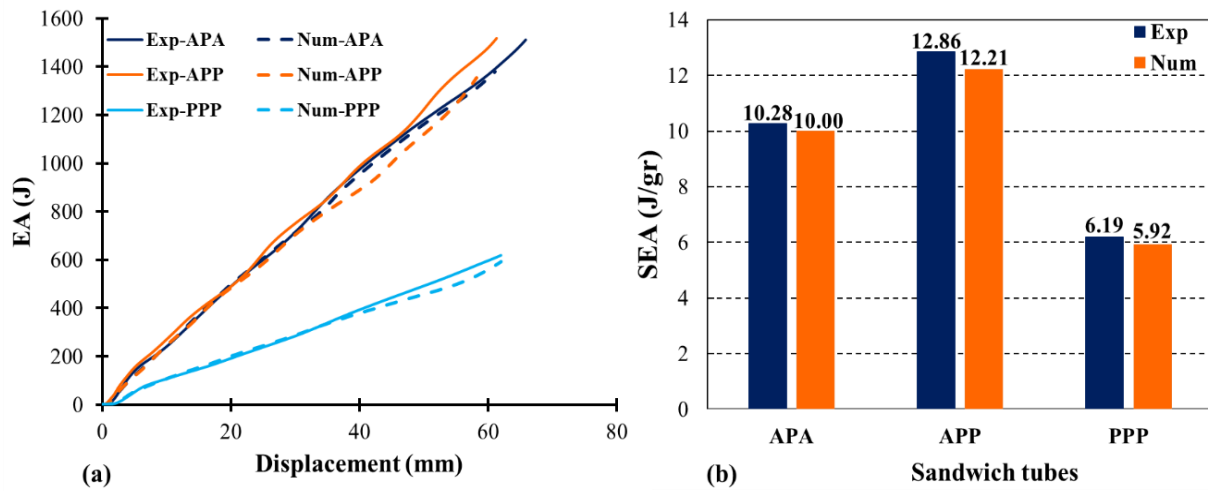
Figure 16 : Comparison of (a) EA and, (b) SEA of sandwich tubes.
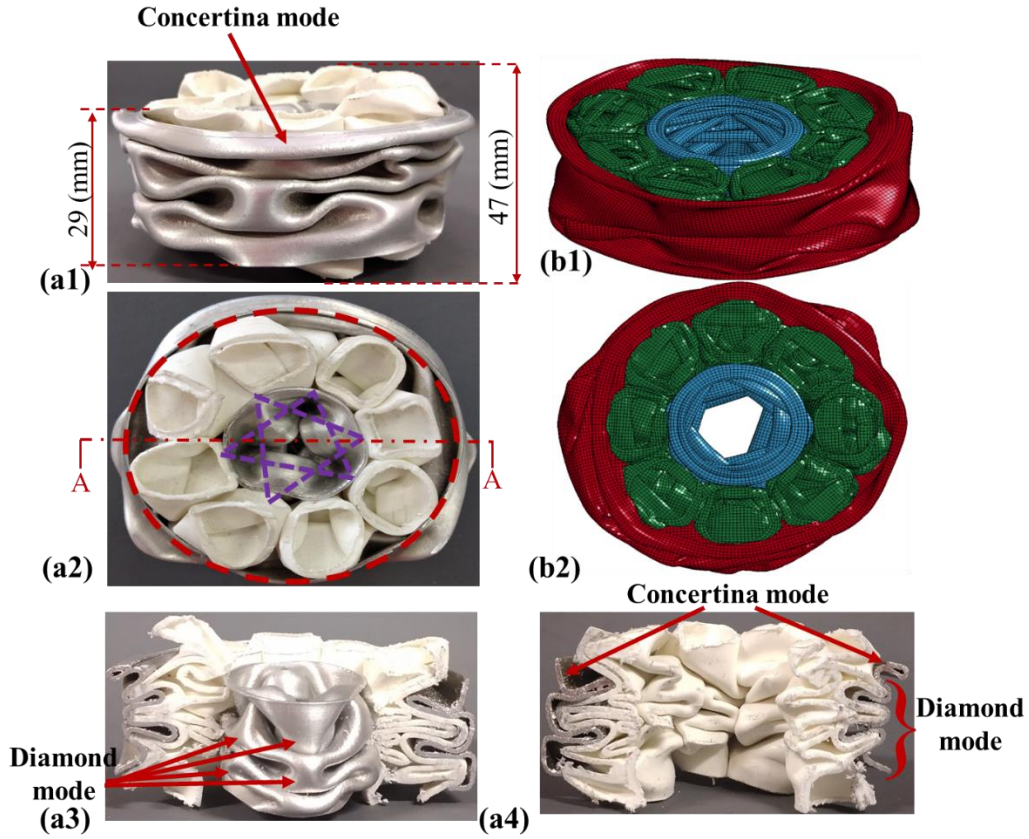
Figure 17 : Comparison of axial crushing modes of APA specimen from the (a) experimental and (b) numerical results.
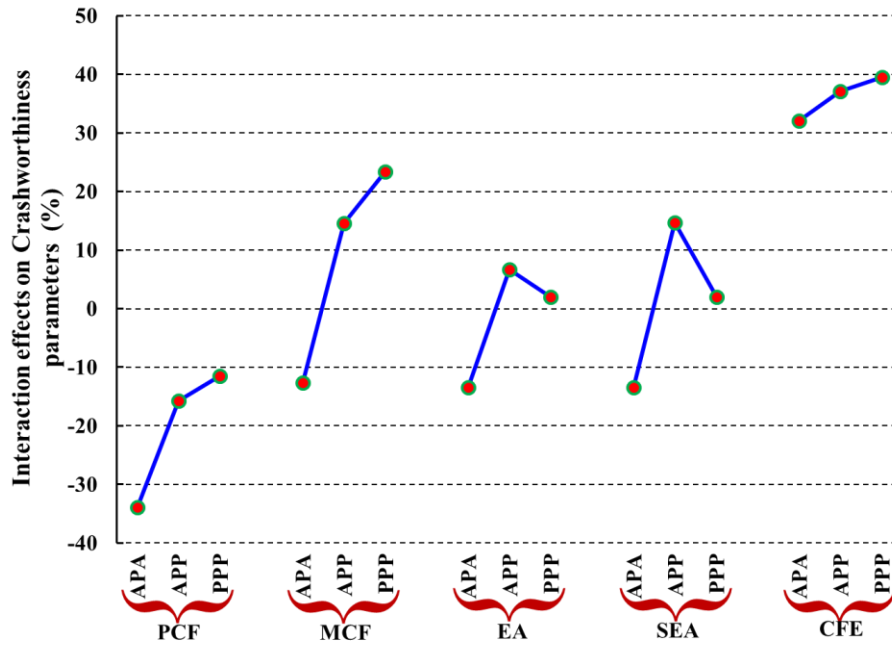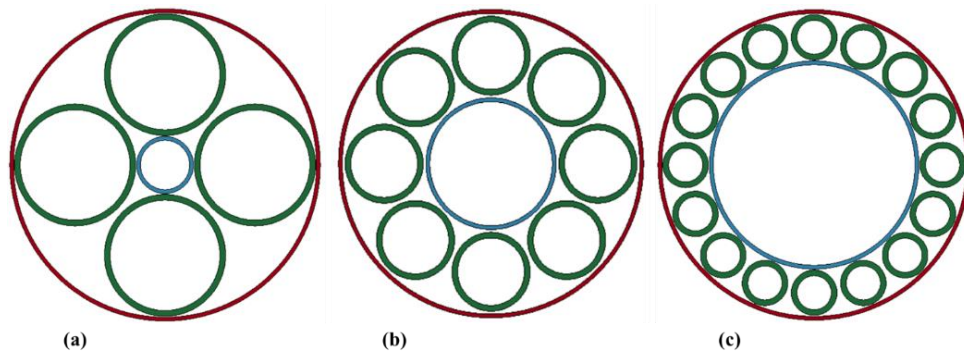

Figure 18: The crashworthiness evaluation indexes of three sandwich tubes and the sum effect of components.
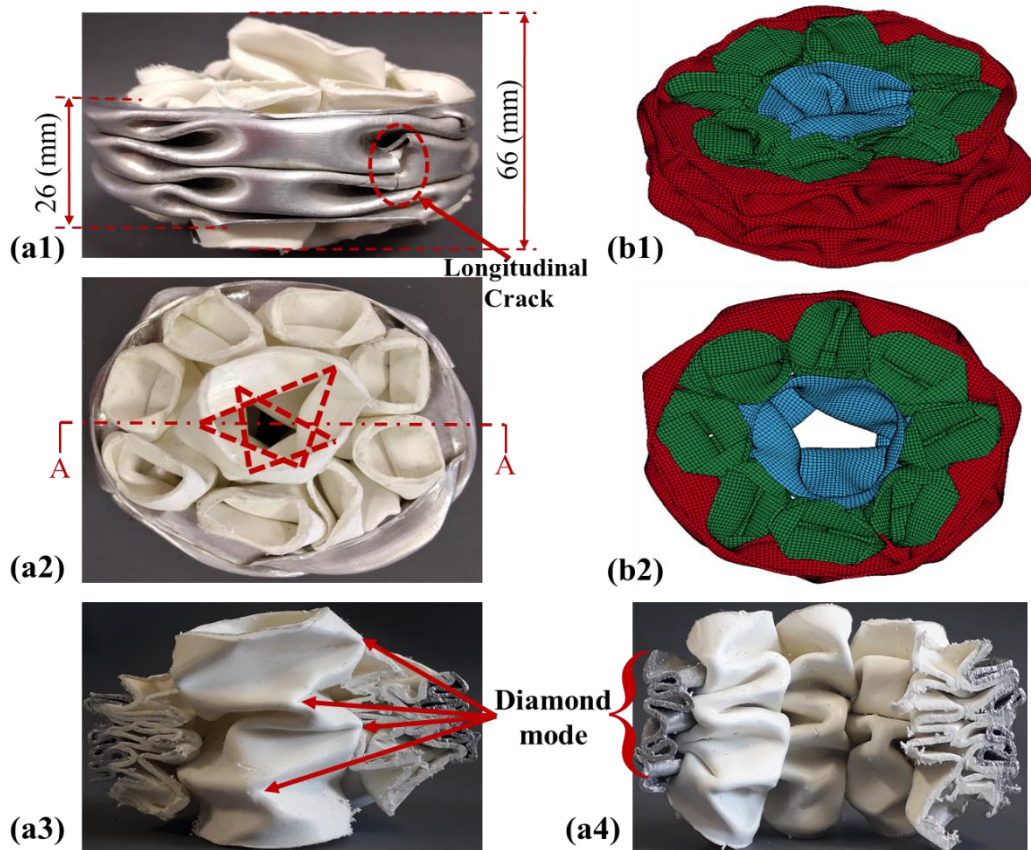
Figure 19 : Comparison of axial crushing modes of APP specimen from the (a) experimental and (b) numerical results.
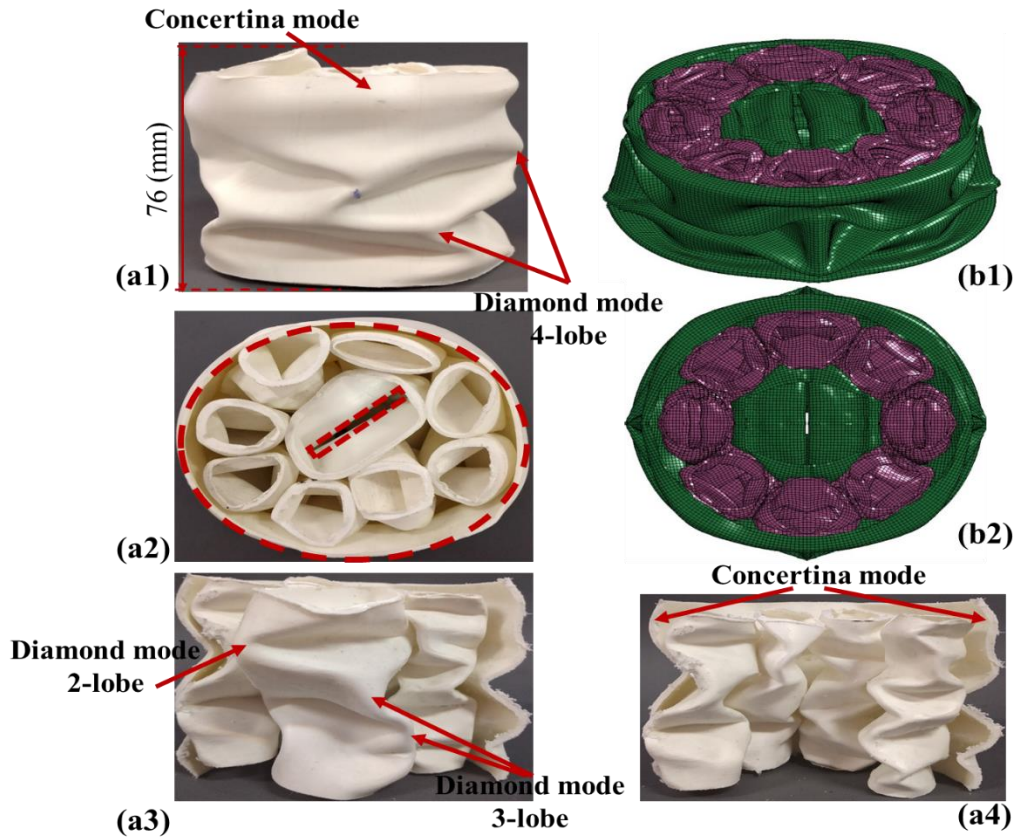
Figure 20 : Comparison of axial crushing modes of PPP specimen from the (a) experimental and (b) numerical results.

Figure 21 : Three configurations corresponding to parametric study: a) config.1, b) config.2, and c) config.3.
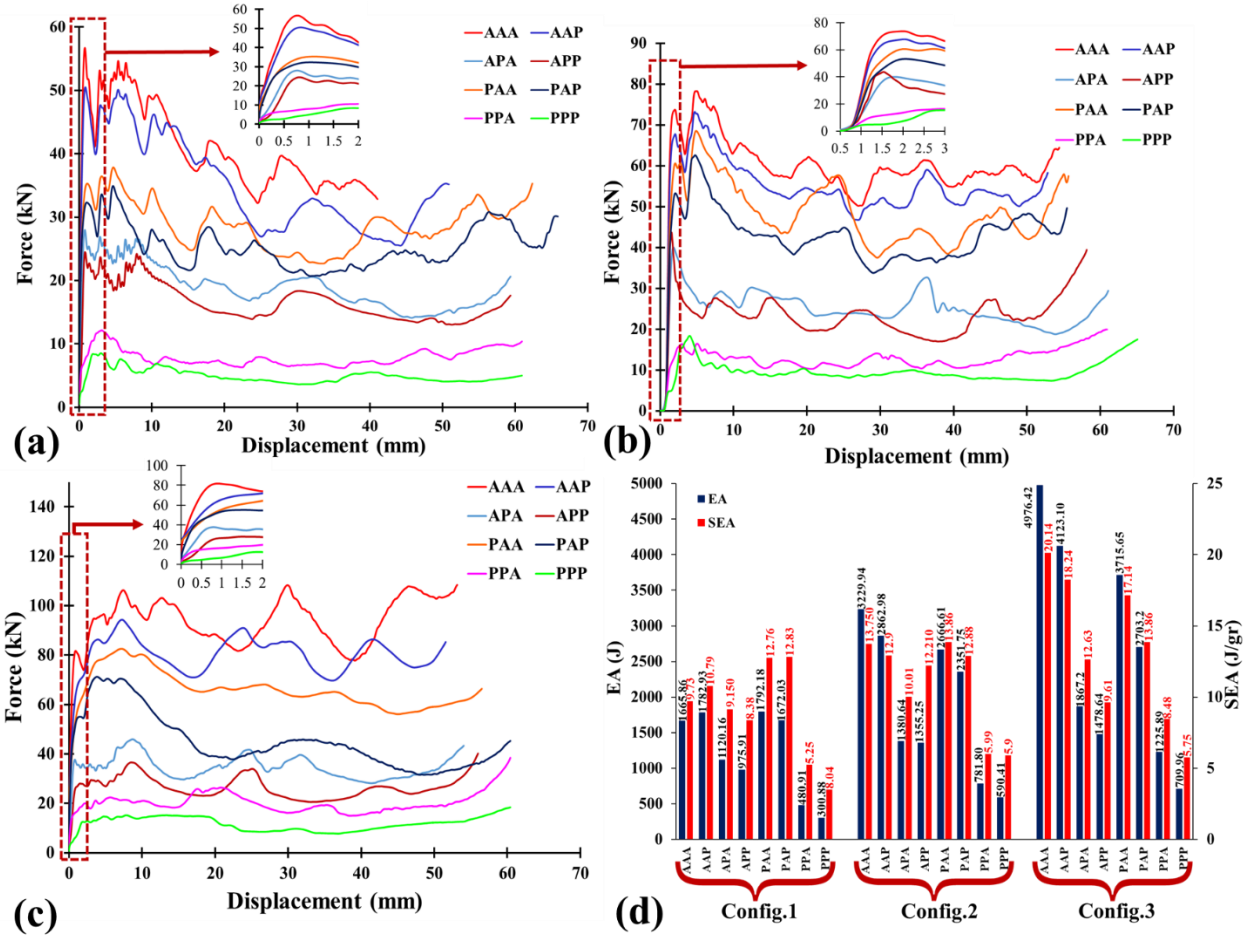
Figure 22 : Comparative load-displacement curves of hybrid multi-cell tubes under study: a) config.1, b) config.2 c) config.3 and d) the calculated EA and SEA corresponding to each sandwich tube.

(a) PAP   (b) PAA   (c) AAA
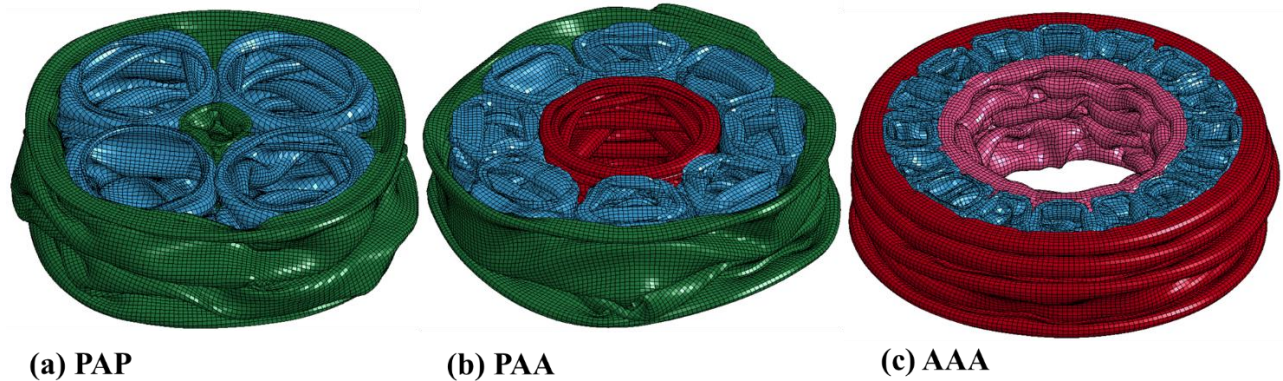
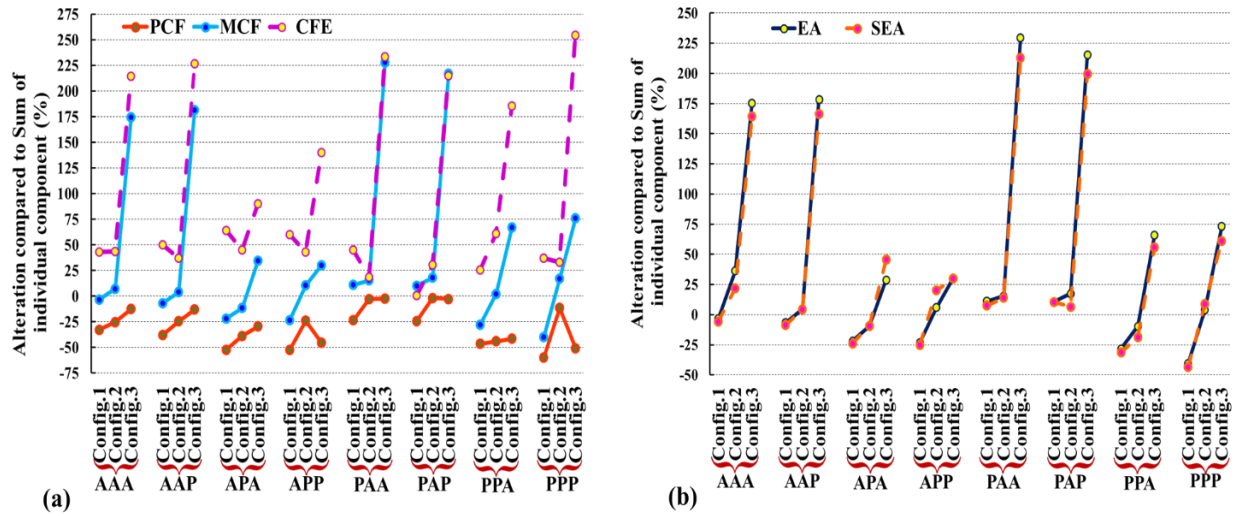Figure 23 : axial crushing modes of specimen with the highest SEA in a) config.1, b) config.2, and c) config.3.

Figure 24 : The crashworthiness evaluation indexes of all sandwich tubes in the numerical study and the sum effect of components, (a) PCF, MCF and, CFE (b) EA and SEA.
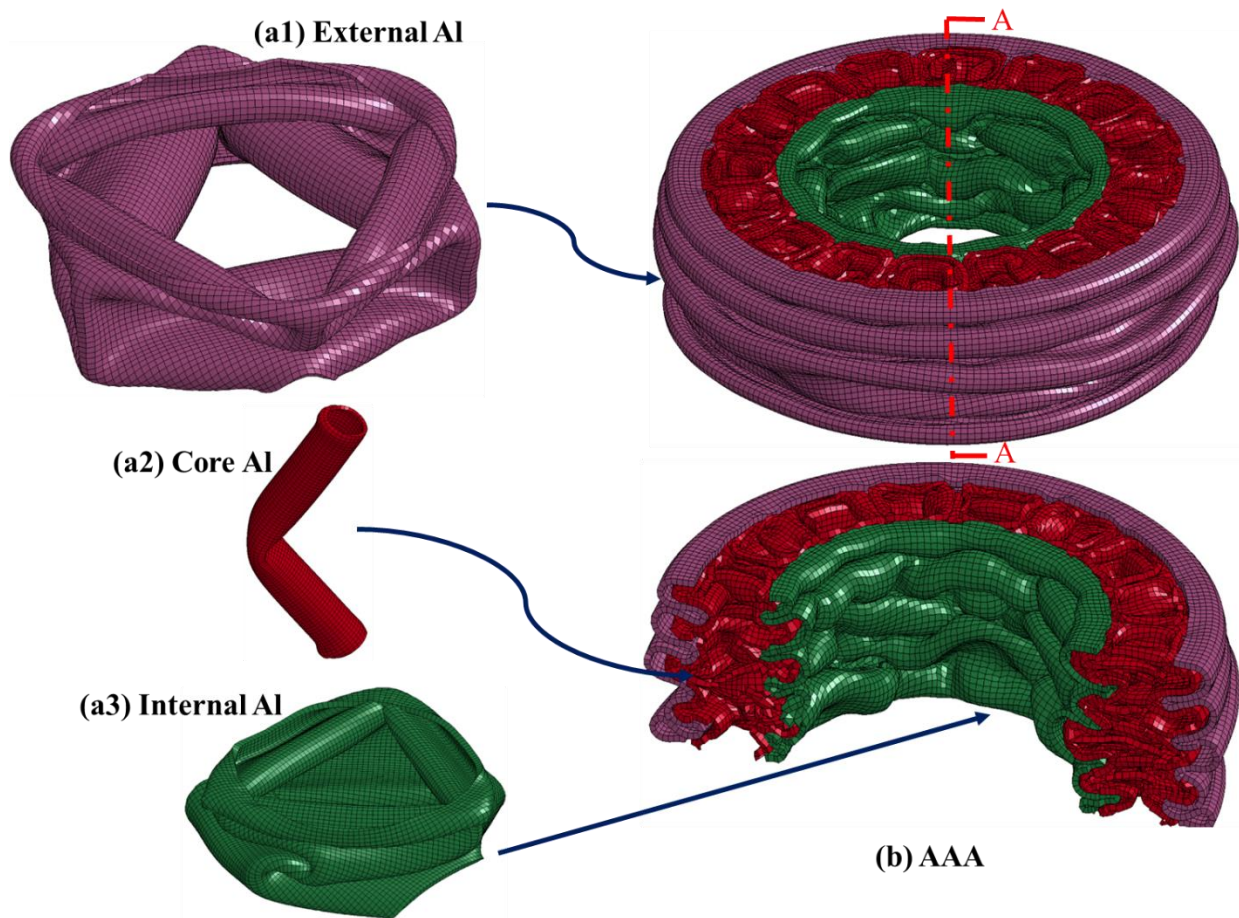

Figure 25 : The effect of interaction in the multi-cell tubes on the (a) single hollow tube collapse mechanism in (b) AAA – config.3.
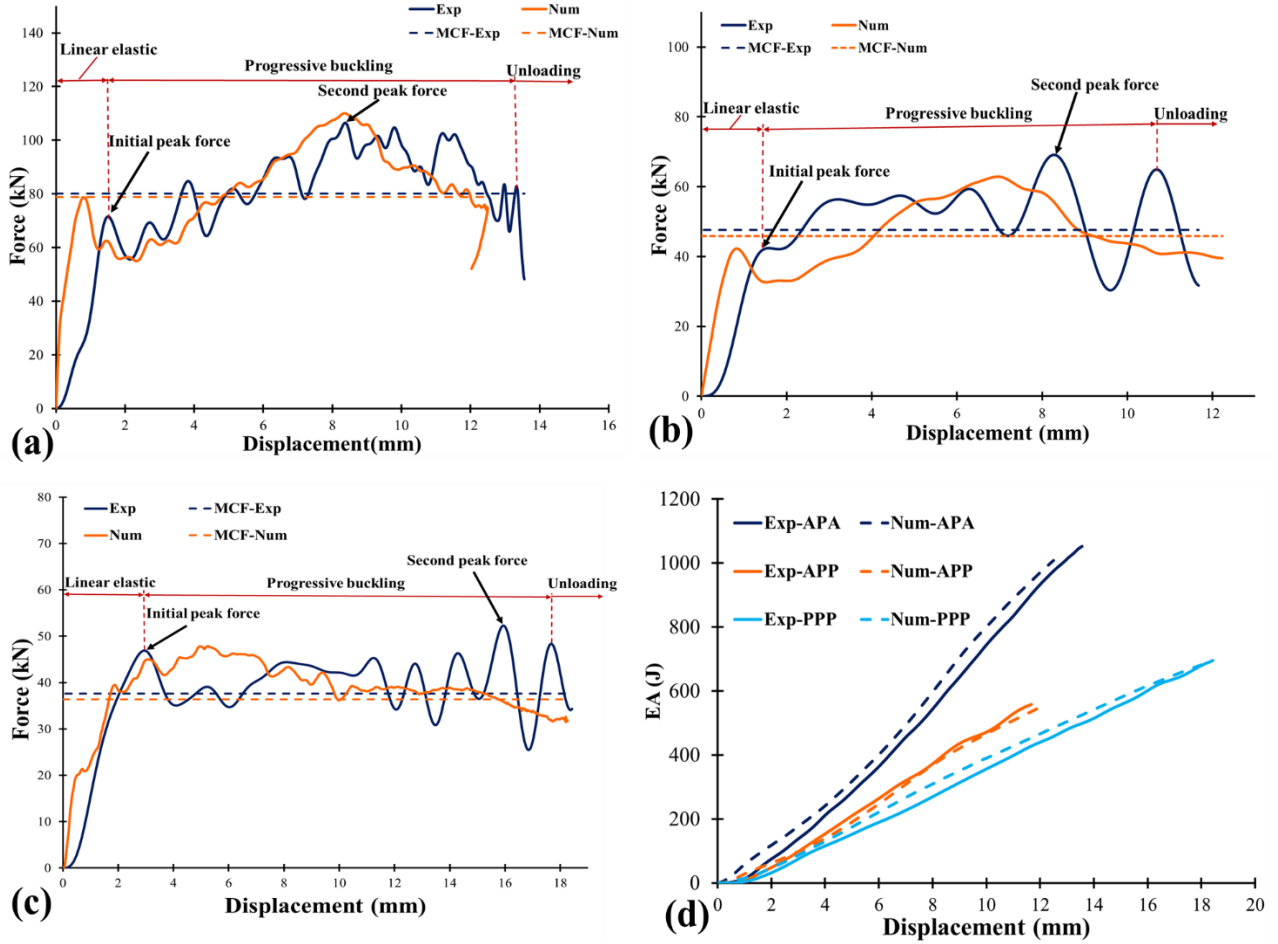
Figure 26 : Load-displacement curves of a) APA, b) APP, c) PPP, and d) corresponding EA curves.
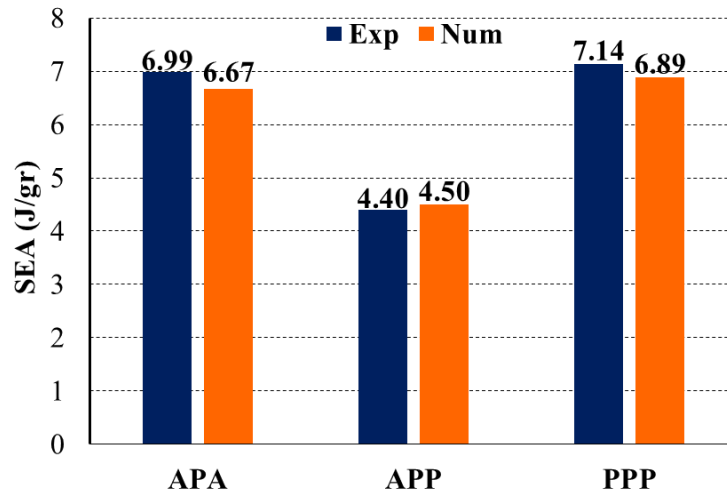

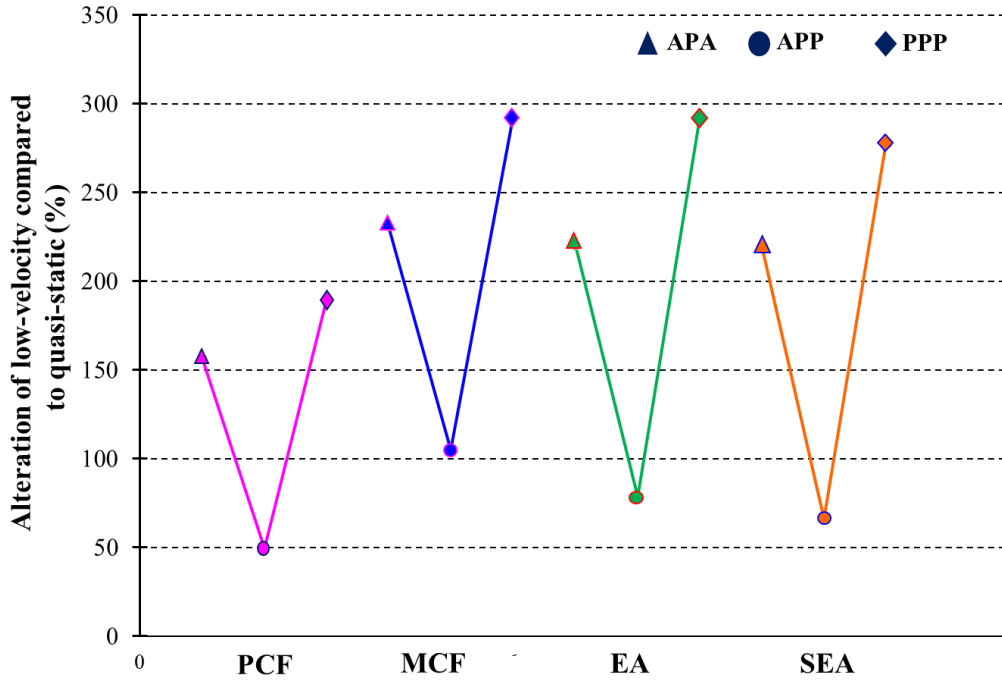Figure 27 : Comparison of SEA of sandwich tubes under low-velocity impact.

Figure 28 : Variations of crush parameters in low-velocity compared to quasi-static conditions.
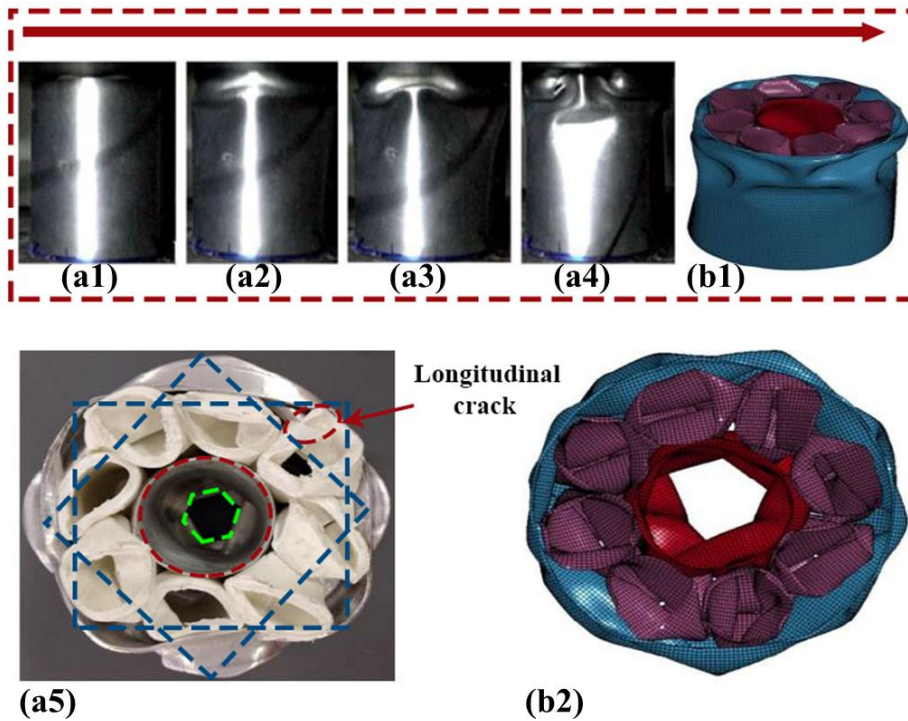

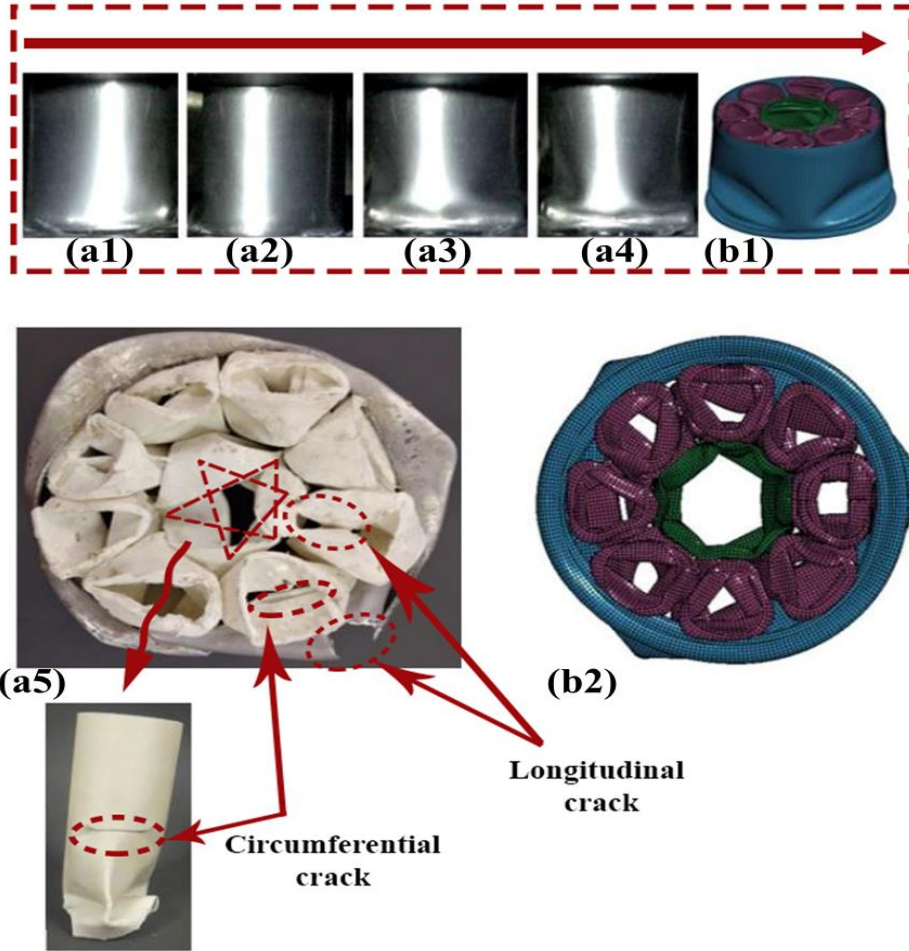
Figure 29 : Status of low-velocity compression of (a) experiments and (b) simulation of APA specimen.

Figure 30 : Status of low-velocity compression of (a) experiments and (b) simulation of APP specimen.

(a1)   (a2)   (a3)   (a4)   (b1)

(a5)

Longitudinal
crack

Circumferential
crack

(b2)
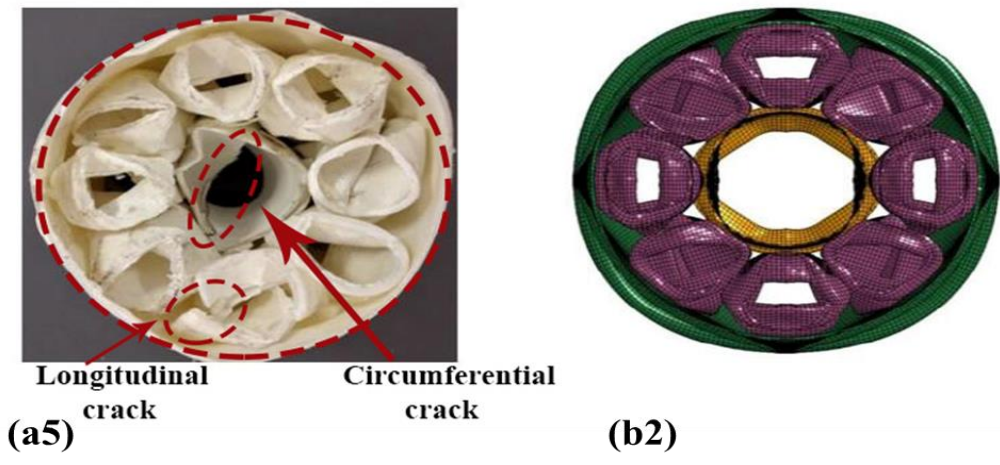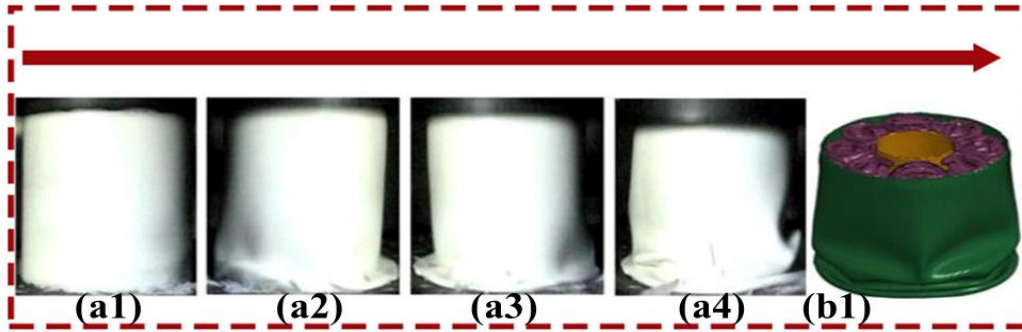
Figure 31 : Status of low-velocity compression of (a) experiments and (b) simulation of PPP specimen.
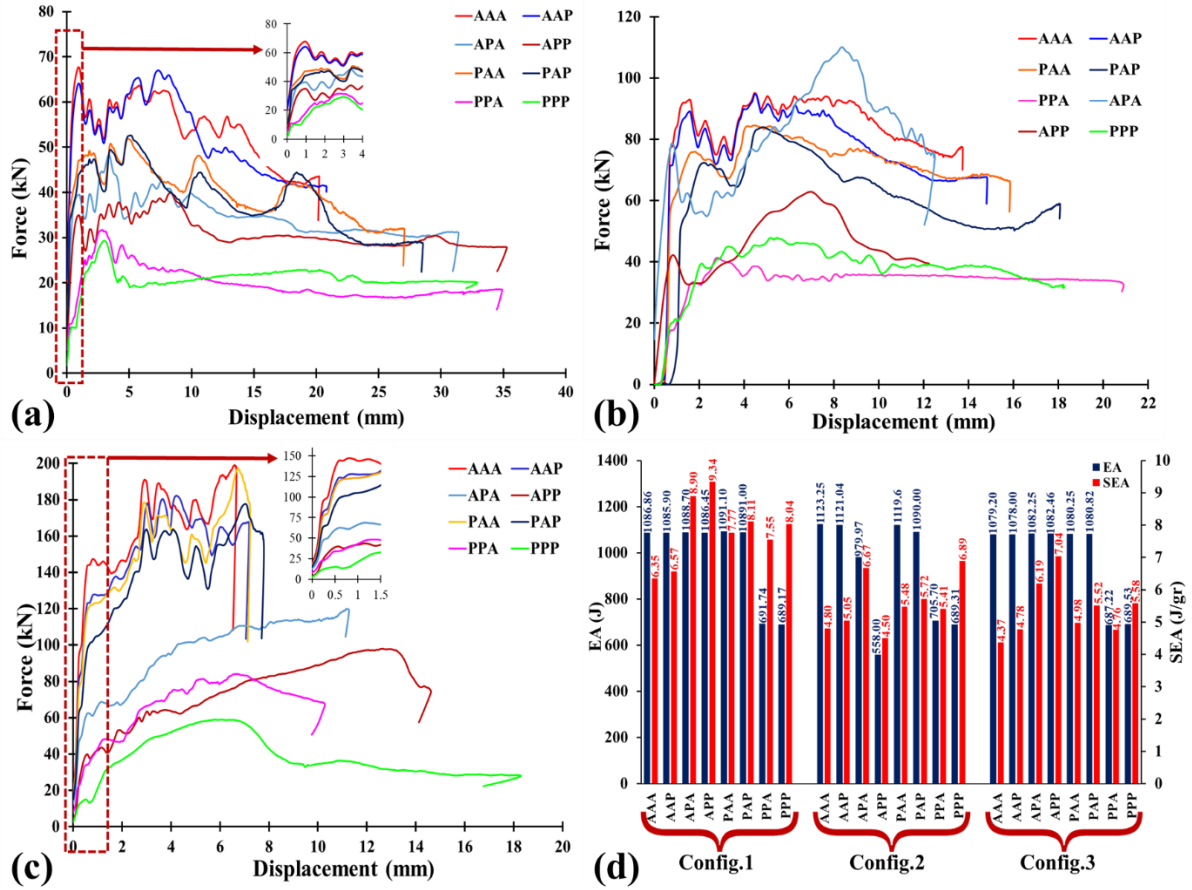
Figure 32 : Comparative load-displacement curves of hybrid multi-cell tubes under study: a) config.1, b) config.2 c) config.3 and d) the calculated EA and SEA corresponding to each sandwich tube.

(a) APP   **(b) PPP**   **(c) APP**
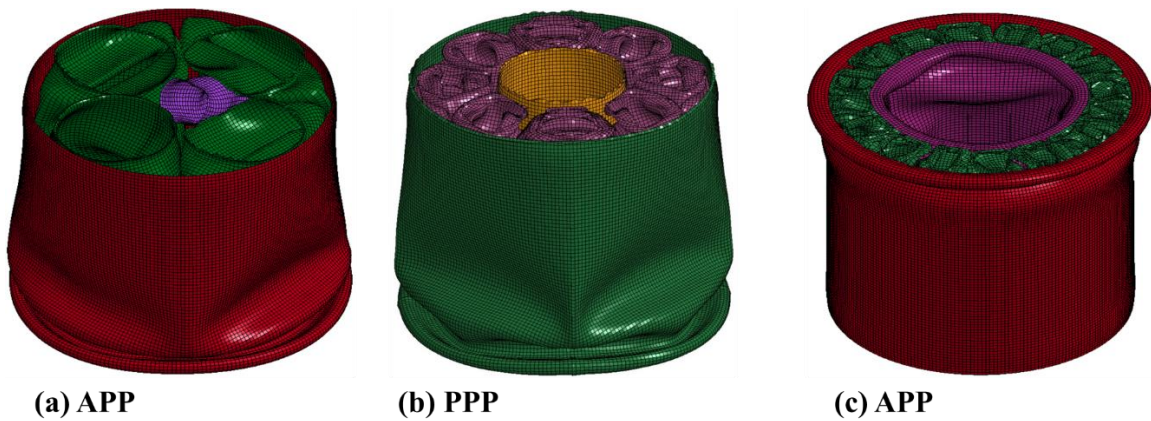
Figure 33 : axial crushing modes of the specimen with the highest SEA in (a) config.1 (b) config.2 (c) config.3.
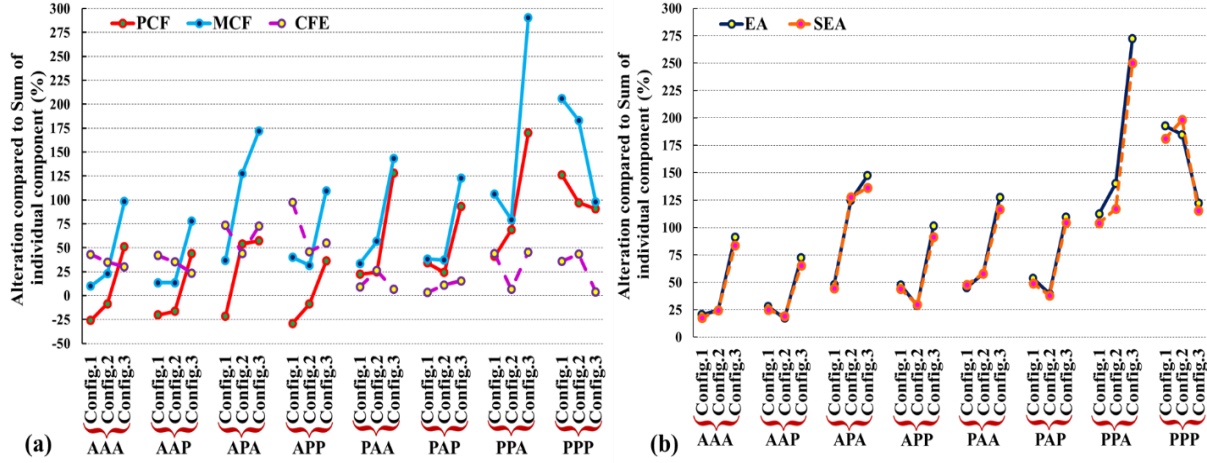
Figure 34 : The crashworthiness evaluation indexes of all sandwich tubes in the parametric study and the sum effect of components, (a) PCF, MCF and, CFE (b) EA and, SEA.

Figure 35 : Comparison of low-velocity to quasi-static variations of crush parameters.

Tables:

Table 1
Mechanical properties of neat polypropylene

Property	Young's moduli (MPa)	yield stress (MPa)	ultimate stress (MPa)	Poisson's ratio
Value	1450	24	28	0.45

Table 2
 (D/t) and (H/D) ratios corresponding to Al and PP tubes.

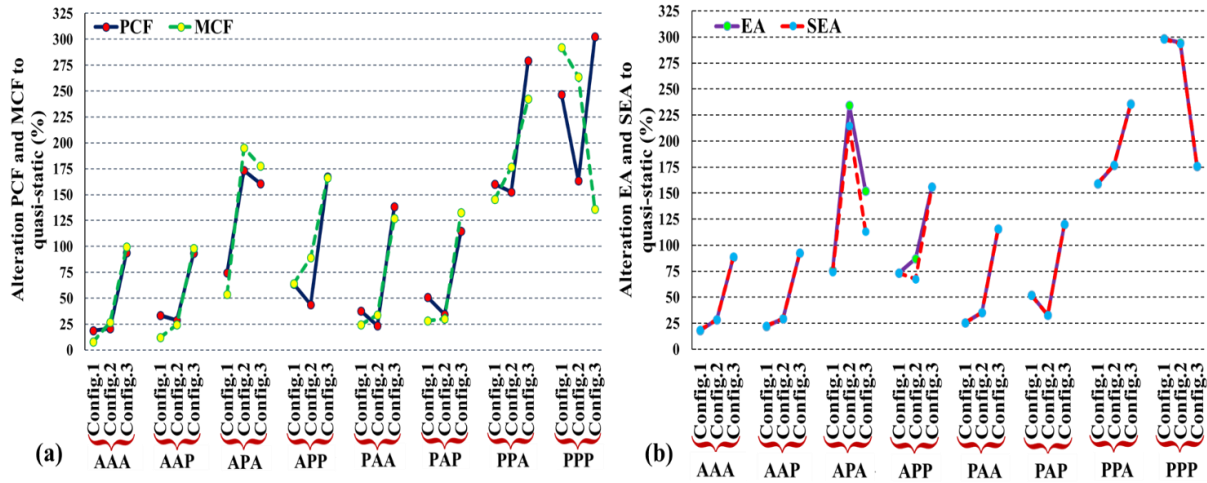|	D/t	H/D
Internal Al	٣٥٫٠	٢٫٥٧
External Al	٨٢٫٠	١٫١٠
Internal PP	٢٣٫٣٣	٢٫٥٧
External PP	٥٤٫٦٧	١٫١٠
Core PP	١٤٫٠	٤٫٢٩

Table 3
Comparison of quasi-static experiment and numerical simulation results of Al tubes.

Specimen	Result	PCF (kN)	MCF (kN)	CFE (%)	CLE (%)
Internal Al	Experimental	١٠٫٤٥	٦٫٦٤	٦٣٫٥	٦٨٫٤
	Numerical	١١٫١٧	٦٫٦٧	٥٩٫٧	٦٦٫٦
	Error (%)	٦٫٤٤	٠٫٤٥	٦٫٠	٢٫٦
External Al	Experimental	٤٠٫١١	١٥٫١٩	٣٧٫٩	٧٥٫٩
	Numerical	٤٢٫٣٩	١٤٫٨٠	٣٤٫٩	٧١٫٠
	Error (%)	٥٫٣٧	٢٫٦	٧٫٩	٦٫٤

Table 4
Comparison of quasi-static experiment and numerical simulation results of PP tubes.

Specimen	Result	PCF (KN)	MCF (kN)	CFE (%)	CLE (%)
Core PP	Experimental	١٫٥٤	٠٫٦٠٤	٣٩٫٢	٧٩٫٣
	Numerical	١٫٥٨	٠٫٥٩	٣٧٫٣	٧٤٫٥
	Error (%)	٢٫٦	٢٫٣	٤٫٥٨	٦٫٤
Internal PP	Experimental	٣٫٠٣	٠٫٩٩	٣٢٫٧	٨٣٫١
	Numerical	٣٫٠٠	١٫٠٢	٣٤٫٠	٧٨٫٩
	Error (%)	١٫٠	٣٫٠	٤٫٠	٥٫١
External PP	Experimental	٥٫١٣	٢٫٣٠	٤٤٫٨	٧٩٫٧
	Numerical	٥٫٤٧	٢٫٣٣	٤٢٫٦	٧٩٫٩
	Error (%)	٦٫٦	١٫٣	٤٫٩	٠٫٢

Table 5
Comparison of quasi-static experiment and numerical simulation results of sandwich tubes.

Specimen	Result	PCF (KN)	MCF (kN)	CFE (%)	CLE (%)
APA	Experimental	۴۱/۵۸	۲۳/۲۵	۵۵/۹۲	۷۳/۱۵
	Numerical	۴۰/۰۲	۲۴/۴۰	۶۱/۰۰	۶۷/۹
	Error (%)	۳/۷	۴/۷	۹/۱	۷/۲
APP	Experimental	۴۶/۳۷	۲۴/۰۵	۵۱/۹۰	۶۸/۱۳
	Numerical	۴۳/۶۸	۲۳/۲۸	۵۳/۳۰	۶۴/۶
	Error (%)	۵/۸	۳/۲	۲/۷	۵/۲
PPP	Experimental	۱۸/۱۲	۹/۹۸	۵۵/۱۰	۶۸/۹
	Numerical	۱۸/۴۰	۹/۵۴	۵۵/۲۰	۶۸/۴
	Error (%)	۱/۵	۴/۴	۰/۲	۰/۷

Table 6
Geometric characteristics of the three configurations defined in the parametric study.

	D internal tube (mm)	D core tube (mm)	Number of core tubes
Config.1	۱۵	۳۲	٤
Config.2	۳۵	۲۱	۸
Config.3	۵۵	۱۲	۱٦

Table 7
Summary of the corresponding crashworthiness parameters of the various hybrid multi-cell tubes configurations.

Configuaration	Material permutation	PCF (kN)	MCF (kN)	CFE (%)	CLE (%)
Config.1	AAA	56.7	40.56	71.53	45.62
	AAP	50.12	35	69.83	56.54
	APA	27.38	18.85	68.84	65.95
	APP	25.72	16.42	63.84	65.95
	PAA	37.48	28.72	76.63	69.29
	PAP	34.49	25.36	73.53	73.21
	PPA	11.98	7.88	65.78	67.7
	PPP	8.32	4.93	59.25	67.7
Config.2	AAA	77.92	59.28	76.08	60.68
	AAP	72.85	54.11	74.27	58.71
	APA	40.02	24.4	61	67.9
	APP	43.68	23.28	53.3	64.6
	PAA	68.05	47.83	70.28	61.87
	PAP	62.08	42.35	68.22	61.62
	PPA	16.08	12.8	79.6	67.71
	PPP	18.4	9.54	55.2	68.4
Config.3	AAA	105.85	93.55	88.38	59.04
	AAP	93.87	79.88	85.1	52.29
	APA	45.46	34.52	75.93	60.04
	APP	36.5	26.39	72.3	62.21
	PAA	82.24	65.69	79.87	62.78
	PAP	71.15	44.7	62.82	67.12
	PPA	25.44	20.28	79.72	67.41
	PPP	14.98	11.74	78.37	67.78

Table 8
Comparison of low-velocity impact experiment and numerical simulation results of sandwich tubes.

Specimen	Result	PCF (kN)	MCF (kN)	CFE (%)	CLE (%)
APA	Experimental	۱۰۵/۷۱	۸۰/۱۷	۷۵/۸۴	۱۵/۰۶
	Numerical	۱۰۹/۸۵	۷۸/۸۰	۷۱/۷۳	۱۳/۸۸
	Error (%)	۳/۹۰	۱/۷	۵/۴	۷/۸۳
APP	Experimental	۶۹/۰۱	۴۷/۶۴	۶۹/۰۳	۱۲/۹۷
	Numerical	۶۲/۸۷	۴۵/۷۸	۷۲/۸۲	۱۳/۵۸
	Error (%)	۸/۹۰	۳/۹	۵/۵	۴/۷
PPP	Experimental	۵۲/۱۷	۳۷/۶۵	۷۲/۲۰	۲۰/۵۱
	Numerical	۴۷/۷۴	۳۶/۳۹	۷۶/۲۲	۲۰/۲۳
	Error (%)	۸/۵	۳/۴	۵/۶	۱/۴

Table 9
Summary of the corresponding crashworthiness parameters of the various hybrid multi-cell tubes configurations.

Configuaration	Material permutation	PCF (kN)	MCF (kN)	CFE (%)	CLE (%)
Config.1	AAA	67.4	49.1	72.85	22.42
	AAP	66.95	47.74	71.31	23.12
	APA	47.9	22.23	46.41	32.77
	APP	40.9	29.19	71.37	39.1
	PAA	51.93	39.73	70.73	32.74
	PAP	52.42	34.01	64.88	29.9
	PPA	31.49	18.75	59.54	38.67
	PPP	29.03	20.54	70.75	36.53
Config.2	AAA	94.61	80.39	84.97	15.26
	AAP	94.1	72.47	77.01	16.43
	APA	109.85	78.8	71.73	13.36
	APP	62.87	45.78	72.82	13.58
	PAA	84.52	69.45	82.2	17.58
	PAP	83.92	58.42	69.61	20.1
	PPA	41.12	33.78	82.15	23.14
	PPP	47.66	36.39	76.35	20.28
Config.3	AAA	197.73	170.52	86.24	7.33
	AAP	182.25	154.15	84.58	7.93
	APA	119.49	104.88	87.77	15.52
	APP	97.61	76.77	78.65	16.2
	PAA	196.69	158	80.33	7.99
	PAP	177.35	145.94	82.29	8.63
	PPA	84.09	67.47	80.23	11.43
	PPP	58.84	32.06	54.45	20.22